University Of Crete

Medical School UOC
Master Thesis

"Development of a Computational Male Pelvis Phantom for the Generation of Multiseries MRI Synthetic Data in Support of Image Analytic Processes."

Graduate Student: Konstantina Giouroukou
Supervisor: Prof. Konstantinos Marias
Advisors: Ms. Katerina Nikiforaki, Mr. George Manikis

December 12, 2023

"The important thing is
not to stop questioning."
Albert Einstein

Acknowledgements

This thesis was conducted at the Computational Bio-Medicine Laboratory (CBML) of the Foundation of Research and Technology (FORTH) as part of the Biomedical Engineering postgraduate program. Firstly, I would like to express my gratitude to Prof. Marias who accepted to be my supervisor and entrusted me with the opportunity to explore a new research world. A big thank you is owed to Mr. Manikis who agreed to collaborate and encouraged me to pursue my research aspirations. This work could not have been accomplished without the invaluable assistance, support, and excellent collaboration with Ms. Nikiforaki. I owe her the majority of this work, as her guidance was more than significant for me. She instilled in me an interest in the physics of MRI, and she was always there for any challenges I faced. I truly feel grateful for the opportunity to participate in a research laboratory and, through an environment of exceptional cooperation, acquire knowledge and experiences that will be assets for my future journey in science and research.

Finally, I would like to sincerely thank my parents for their support throughout all these years. To my sisters, who have been my pillars and sources of inspiration. To my friends, with whom I share common concerns. Special thanks to George; our scientific discussions have been a wellspring of inspiration. I am also indebted to Sophie, who taught me the belief that there is a solution to every challenge. And, last but not least, to Stelios and Eva, who taught me not to give up, to set goals, and to see them through.

Abstract

In this thesis, we utilize existing tools to simulate a data acquisition process and extend their capabilities to a virtual phantom with human anatomy characteristics. Our proposed method involves the creation of a computational male pelvic phantom and the utilization of advanced software to simulate magnetic resonance imaging (MRI) processes, by solving Bloch equations. This work has the potential for important future applications regarding the address of standardization challenges in radiomics, contributing to explainability, robustness, and repeatability in the extraction of radiomic features.

To accurately represent pelvis anatomy, we employed clinical MRI images, leveraging the benefits of tomography and advanced medical image processing techniques. Specifically, we employed segmentation and labeling methods to delineate and differentiate each tissue, faithfully reproducing the spatial distribution of muscles and fat—the primary components constituting the pelvis. In MRI, each tissue exhibits distinct parameters such as T1, T2, T2*, and proton density, which are related to the signal and the intrinsic contrast of each tissue. In this study, we assigned tissue properties that relied on established values from the literature. For simulation purposes, we utilized the specialized MRI simulator software, MRiLab. The implementation of the fundamental clinical sequence, Spin Echo (SE), coupled with the investigation of three distinct contrasts (T1-weighted, T2-weighted, and proton density-weighted), forms a well-examined study. In our experimental results, we showcase the MRI images generated through the simulation of the male pelvic phantom and highlight specific applications in image analysis.

The methodology employed for phantom creation can be extended for deployment in any body region, allowing the digital reproduction of patient-specific or requested anatomical structures for various research studies. Leveraging the MRI simulator facilitates the application of clinical MRI protocols and the generation of necessary image data-sets. The potential applications and versatility of our phantom are extensive, spanning from computational measurements and physics estimations to the generation of synthetic data for training artificial intelligence models. Furthermore, its utility extends to preclinical trials and educational purposes. In conclusion, our phantom could be valuable in radiomic analysis. Its application emerges as a potential solution to standardization challenges in radiomic features and facilitates a comprehensive examination of variability issues across various clinical protocols.

Περίληψη

Σε αυτήν την εργασία προτείνουμε την δημιουργία ενός υπολογιστικού phantom το οποίο θα αναπαριστά την ανατομική περιοχή της ανδρικής πυέλου και την χρήση ενός καταρτισμένου λογισμικού για την προσομοίωση εικόνων μαγνητικής τομογραφίας. Ένας βασικός στόχος στο μέλλον είναι η χρήση των υπολογιστικών phantom σαν μέθοδο κανονικοποίησης για την εξαγωγή ραδιομικών χαρακτηριστικών.

Για την αναπαράσταση της ανατομίας της πυέλου χρησιμοποιήσαμε πραγματικές εικόνες μαγνητικής τομογραφίας, εκμεταλλευόμενοι το πλεονέκτημα της τομογραφίας και των τεχνικών επεξεργασίας ιατρικών εικόνων. Πιο συγκεκριμένα εφαρμόστηκαν μέθοδοι κατάτμησης και επισήμανσης για την οριοθέτηση και τον διαχωρισμό κάθε ιστού, αναπαράγοντας την ανατομία του μυός και του λίπους, των κυριότερων ιστών που συνθέτουν την πύελο. Στην μαγνητική τομογραφία κάθε ιστός χαρακτηρίζεται από συγκεκριμένες παραμέτρους όπως είναι οι T1, T2, T2* και η πυκνότητα προτωνίων, οι οποίες σχετίζονται με το σήμα και το εγγενές contrast κάθε ιστού. Οι τιμές που ανατέθηκαν στις παραμέτρους κάθε ιστού προήλθαν από την διεθνή βιβλιογραφία. Για τις ανάγκες της προσομοίωσης χρησιμοποιήσαμε το καταρτισμένο λογισμικό MRiLab. Εφαρμόστηκε η βασική κλινική ακολουθία Spin Echo (SE) και εξετάσθηκαν τρία διαφορετικά contrast (T1w, T2w, PDw). Στα αποτελέσματα μας παρουσιάζουμε τις εικόνες που αποκτήσαμε καθώς και ορισμένες εφαρμογές στην ανάλυση εικόνων.

Η τεχνική που ακολουθήθηκε για την δημιουργία και τον σχεδιασμό του phantom, δίνει την δυνατότητα κατασκευής οποιασδήποτε ανατομίας και μας επιτρέπει να αναπαράγουμε ψηφιακά οποιονδήποτε ασθενή ή ανατομία μας ζητηθεί για ερευνητικούς σκοπούς. Με την χρήση του προσομοιωτή μαγνητικής τομογραφίας μας δίνεται η ευκαιρία να εφαρμόσουμε κλινικά MRI πρωτόκολλα και να παράγουμε οποιοδήποτε σύνολο δεδομένων. Οι εφαρμογές του phantom μας είναι αμέτρητες, από την χρήση του για υπολογιστικές μετρήσεις ή εκτιμήσεις στον τομέα της φυσικής και την δημιουργία συνθετικών δεδομένων για την εκπαίδευση AI μοντέλων μέχρι και την χρήση του για προ-κλινικές δοκιμές και εκπαιδευτικούς σκοπούς. Τέλος ιδιαίτερο ενδιαφέρον θα έχει η χρήση του phantom στην ραδιομική ανάλυση, όπου φαίνεται πως η χρήση του μπορεί να προτείνει λύση στο ζήτημα κανονικοποίησης των ραδιομικών χαρακτηριστικών καθώς και να εκτιμήσει ζητήματα μεταβλητότητας μεταξύ κλινικών πρωτοκόλλων.

CONTENTS

LIST OF FIGURES

Introduction

Undoubtedly, the clinical magnet stands as a 21st-century innovation, playing an active role in global health through advancements in diagnostic imaging and treatment planning. The intricacies of its design, encompassing both hardware and software components, coupled with the signal's dependence on external parameters, highlight the challenge of variability in images produced by clinical MRI. To address this concern, excluding the variability induced by the imaging subject, medical physicists study imaging phantoms, which are crucial for MRI machines calibration as well as contribute to diverse computational research measurements, such as relaxometry.

This work is grounded in the imperative need to establish computational phantoms for estimating and addressing issues of standardization related to acquisition practices of MRI images. The concept of constructing a computational human phantom and leveraging an MRI simulator for image generation emerges as a valuable approach to tackle the challenges associated with variability in MRI images.

Our work revolves around two primary objectives: the construction of a male pelvic phantom and its subsequent utilization for MRI experiments based on virtual scanning. In the upcoming chapters, we extensively explore the role of imaging and computational phantoms in medical imaging. We detail the techniques employed for designing the phantom, underscoring our dedication to accurately replicate real tissue anatomy. The simulation phase was executed with the software tool, MRiLab, chosen for its optimal alignment with our experimental objectives. Furthermore, a fundamental aspect of our study involved acquiring a comprehensive understanding of MRI, including its clinical protocols. This knowledge proved instrumental, particularly in the application of the basic Spin Echo (SE) sequence for image acquisition.

In the results section, we present both the experimental images and the corresponding imaging parameter tables. The adaptability of our approach, allowing the generation of anatomical regions with precise physical properties, equips us with the capability to create diverse image datasets. These datasets can serve various scientific purposes, enabling data mining across a range of scientific fields. Moreover, the utilization of an MRI simulator facilitates the application of different MRI sequences and protocols, generating synthetic data valuable for advanced studies in artificial intelligence and radiomics.

CHAPTER 1

MRI CHALLENGES AND COMPUTATIONAL PHANTOMS

In the first chapter of this thesis, we will explore the challenges faced in clinical MRI and medical image analysis, focusing primarily on the issue of variability among MRI scanners. To address this challenge, radiologists and researchers employ imaging phantoms to calibrate their imaging procedures.

We will present the concept of imaging phantoms and emphasize the importance of designing and studying computational human phantoms. As a next step, two computational methods for representing human phantoms will be introduced, exploiting the advancements in tomography. Finally, we will highlight the advantages that computational human phantoms bring to MRI research and medical image analysis.

1.1 Challenges in MRI Imaging

Medical Imaging Resonance (MRI) is an imaging technique that exploits strong magnetic fields and radio waves to generate images of human tissues. The source of the MRI signal is the hydrogen nuclei, which can be found in the human body in the form of water or bounded in fat, muscle, proteins etc. MRI is widely used in medical diagnosis to visualize soft tissues, fat, muscle, and fluids. It provides images of high resolution and contrast, without the deposition of ionizing radiation. With MRI images, physicians can detect many abnormalities in the abdomen, and pelvis, neurological disorders, as well as tumors, and musculoskeletal diseases. Another advantage of MRI scanners is that can depict the human body in each geometrical plane, providing 2D or 3D images.

To receive an image with a high diagnostic value requires a well-trained operator, as the procedure of imaging includes handling many parameters that have an impact on the resulting image. The parameters and the different MRI sequences responsible

for image contrast and resolution are discussed in detail in Chapter 3. It must be noted that depending on the operator and the type of MRI sequence we can receive different images for the same anatomical region within a single patient, this is referred to as variability.

Conducting successive MRI scans on the same patient using identical MRI protocols will reveal slight variations in the acquired images. These discrepancies could be attributed to various factors, such as the patient's own condition, the operator performing the examination, or even the MRI scanner itself. A possible effect is the patient's hydration level or motion, which affects the resulting image. In addition, operator skill and technique may contribute to variations in imaging results, as small differences in position or settings may affect the resulting image. Also, as a complex technological system, the scanner machine itself may introduce small variations in image quality or characteristics between different scans. We conclude that MR signal is measured in arbitrary units, it does not represent a physical tissue property and is highly dependent on the statistical nature of the signal. Therefore, it is important to consider and handle these factors when comparing imaging results.

Furthermore, it is worth noting that even when comparing images obtained from different scanners, variations in the final image can occur. This is primarily because each manufacturer employs different magnets, coils, and imaging technologies in their machines. These variations in hardware components and imaging techniques can lead to differences in image quality, resolution, contrast, and other visual characteristics. Consequently, when comparing imaging results from different scanners, it is important to consider the potential influence of these technical differences, as they can contribute to discrepancies in the final image appearance.

Researchers have recognized the challenges associated with various MRI scanning machines and have therefore begun to develop and manufacture phantoms for evaluation purposes. These phantoms offer several advantages, enabling researchers to quantify differences between different MRI machines and serve as invaluable testing tools.

1.2 The Imaging Phantom

An imaging phantom, commonly referred to as a "phantom", is a specially designed device with known geometry and composition that utilized in biomedical research to consistently produce reliable outcomes across various medical imaging

Figure 1.1: The ACR MRI Phantom, which is employed in clinical practice to ensure the quality of MRI scanners for quality assurance purposes.

machines [7]. MRI phantoms consist of materials that replicate the properties of human tissue, behaving similarly to actual human tissues and organs under MRI conditions. As quantitative MRI gains prominence alongside qualitative MRI, it becomes essential to evaluate the stability of imaging systems and comprehend the comparability of measurements obtained across different MRI scanners. A solution seems to be the existence of standard imaging phantoms, that can be used to characterize or calibrate the imaging scanners [8].

The American College of Radiology (ACR) has introduced the "ACR MRI Phantom", specifically designed for assessing and ensuring the performance and quality of imaging equipment, as illustrated in Figure 1.1. It is a cylinder made of acrylic plastic, containing a solution comprising nickel chloride and sodium chloride. The internal dimensions of the phantom measure 148 mm in length and 190 mm in diameter [9]. Inside the phantom are several structures that are necessary to test the scanner performance. This phantom includes a standardized set of test objects that imitate the characteristics of human tissues, aiding in the evaluation of the MRI system's capacity to generate precise and high-quality images [9].

The use of phantoms has a main importance in medical imaging as they can be used for the calibration and quality control of MRI scanners. They can evaluate the scanner's performance by examining its accuracy and reliability. Additionally, phantoms can be employed for the purpose of standardization and comparison among MRI scanners located in different medical centers or manufactured by different companies.

This helps in evaluating advancements in MRI technology and ensuring consistency in imaging results. Another advantage of phantoms in MRI is their use for the development and optimization of MRI sequences. They are used for testing different sequences and helping in the optimization of MRI protocols to enhance image resolution, contrast, and diagnostic accuracy. Artifacts are common in MR imaging, as it is a very demanding scanning process that requires skilled and well-trained operators. Scanning phantoms, researchers can test the scanning parameters and solve or find some strategies to deal with these artifacts.

1.3 Computational Human Phantoms

The computational human phantom is comprised of compartments that simulate the anatomical distribution of various tissues. Since the 1960s, the field of radiological science has been creating and utilizing computational human phantoms, which were first employed in the analysis of ionizing radiation exposure. Over time, significant improvements have been made in these models, enhancing their precision in depicting the internal structure of the human body [10].

In the development of a computational human phantom (CHP), various critical considerations come into play, including anatomical accuracy, tissue characteristics, computational efficiency, and alignment with simulation software [11]. The initial step involves creating a phantom by explicitly defining the surfaces and tissue properties of the relevant bodily tissues where interactions take place. To delineate tissue surfaces, two predominant modeling techniques have been extensively employed:

a. Constructive Solid Geometry (CSG): This established technique involves combining simple geometric shapes and operations to construct complex tissue structures within the phantom.

b. Boundary Representation (BREP): Another well-established method, BREP represents surfaces as a collection of boundary elements, facilitating the description of intricate tissue surfaces.

1.3.1 Constructive Solid Geometry (CSG)

Within the Constructive Solid Geometry (CSG) modeling approach, researchers have the capability to generate solid geometric entities by combining basic shapes referred to as "primitives" [11]. These primitives are defined by quadratic equa-

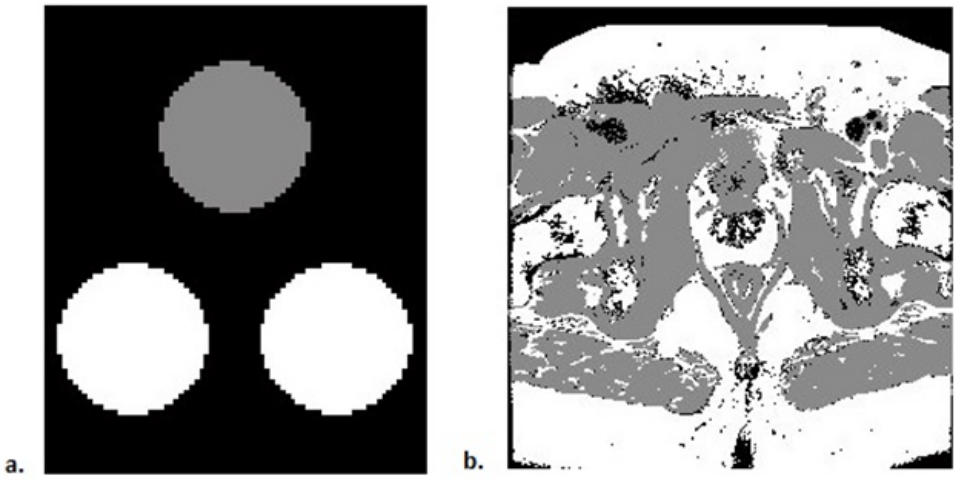

Figure 1.2: a) simple geometries are presented, specifically spheres simulating fat, muscle, and water tissues. These phantoms were created using the MRiLab software tool, which utilizes the Constructive Solid Geometry (CSG) modeling approach and allows the user to create any basic geometry and assign tissue characteristics to it. b) depicts the 2D phantom of the male pelvic region that we designed, where fat and muscle characteristics have been assigned to their corresponding anatomical regions. For this study was generated a three-dimensional (3D) male pelvic phantom with 512x512x22 dimensions, leveraging authentic data sets obtained from an MRI modality.

tions and encompass various fundamental geometric forms such as cuboids, cylinders, spheres, etc. (Figure1.2a).

For instance, the first phantoms employed by the ICPR in the late 1950s depicted organs as spheres and aimed to assess the radiation doses to organs caused by the presence of radioactive materials in both workers and patients [12]. Moreover, the MIRD phantom was the first anthropomorphic phantom [13] that incorporated 22 organs and over 100 sub-regions of the human body. While this model served as the basis for several studies, it provided only a basic overview of the position and geometry of each organ.

The advancements in computer technology and the refinement of tomographic imaging modalities (CT/MRI) give birth to "voxelized phantoms", using voxels as CSG designing techniques. From diagnostic data, we employ image processing methods to convert the human body into a realistic digital 3D representation. In addition, the voxel's geometry is handled easily from the existing simulation codes.

In this study, we utilized this approach to create a phantom of the male pelvic area (Figure 1.2b). Our dataset consisted of 22 MRI images, each with dimensions of 512x512 pixels, provided by the General Hospital of Crete in Heraklion. The images

were segmented properly and then assigned tissue properties to these segmented objects. In the context of MR imaging, each tissue is defined by a specific set of parameters. By assigning the appropriate tissue characteristics to each region, we can label the corresponding region with its respective tissue type. Contrary to physical phantoms, computational human phantoms are scanned in digital MRI simulators.

A limitation of "voxelized phantoms" is evident in their voxel boundaries, which present a jagged, stair-stepped surface rather than a smooth one. Consequently, the precision of anatomical details depends on the voxel size, which can be problematic, especially when dealing with extremely thin and small tissues.

1.3.2 Boundary Representation (BREP)

Advanced modeling techniques within the Boundary Representation (BREP) framework, involving non-uniform rational B-spline (NURBS) surfaces and polygon meshes, offer a sophisticated means of defining human anatomy. BREP-based phantoms are created by extracting organ surface contours from tomographic image data, resulting in smooth and anatomically faithful representations. These versatile models can encompass complex anatomical details. Unlike the Constructive Solid Geometry (CSG) approach, BREP offers greater flexibility, supporting a wide range of operations and surface deformations. This flexibility proves invaluable for adjusting organ size, simulating organ motion, and modifying phantom postures [11]. Despite advancements in digital phantom design that include 4D representations using non-uniform rational B-splines (NURBS) equations and polygon meshes, the "voxelized phantom" approach proved ideal for achieving our objective in this research project.

1.4 Advantages of CHPs in MRI Imaging

A computational human phantom enhances the advantages of MR imaging research, as provides realistic images for MRI evaluation. The computational phantom design is based on real patient image datasets, where we can achieve a very good representation of the human body with the appropriate segmentation method. By utilizing the CHP, we can individually examine each patient, identifying the optimal parameters and sequences that enable accurate visualization of their specific condition. This approach allows for a tailored analysis, ensuring that the appropriate imaging parameters and sequences are employed to effectively capture and interpret

the patient's unique characteristics and pathology, steering to better diagnosis and treatment planning.

Furthermore, the utilization of a CHP in conjunction with an MRI simulation platform has the potential to generate substantial datasets comprising MRI images. These datasets can be created by experimenting with various sequences employed in clinical MRI or by simulating diverse pathologies and MRI machine protocols. Consequently, a comprehensive dataset can be established for the purpose of conducting AI experiments, with a particular focus on the analysis of pathologies and the variability inherent in MRI machines.

CHAPTER 2

THE MALE PELVIC

In this study, we created a computational phantom of the male pelvic area, which refers to the anatomical region in the lower part of the male body. Specifically, we simulated the regions encompassing muscle and fat within the male pelvic foot. In this chapter, we will explore the anatomy of the male pelvic foot and briefly introduce the three distinct muscle layers that comprise it.

Based on numerous scientific researches, MRI has proven to be a valuable tool for detecting and diagnosing various health issues in the male pelvic area [14] [15]. It enables healthcare professionals to identify tumors and abnormalities, with exceptional clarity and detail due to its high-resolution images.

Notably, it has emerged as an indispensable resource for the diagnosis and strategic planning of interventions for prostate cancer [16] [17] [18] —a prevalent condition among men, ranking as the most frequently diagnosed cancer aside from skin malignancies. On a global scale, statistics from 2020 reveal that an estimated 1,414,259 men were diagnosed with prostate cancer, making it the fourth most frequently diagnosed cancer worldwide [19].

2.1 Male Pelvic Floor Anatomy

The male pelvis comprises the structures and organs located within the pelvic cavity and plays a pivotal role in numerous essential functions, including digestion, urination, and reproduction, as well as providing support for the lower abdomen and pelvic organs (Figure 2.1).

Understanding the anatomy of the pelvic floor is essential for correctly interpreting imaging scans of this region, especially in male patients. The male pelvic floor

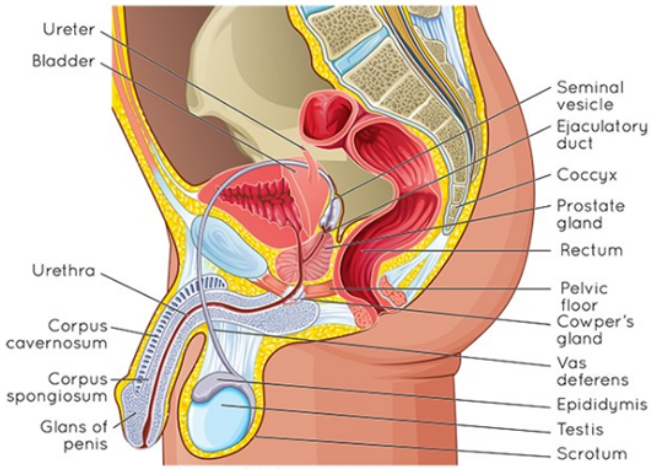

Figure 2.1: Anatomy of the male pelvic region, showcasing the fundamental organs pivotal to its physiological functions.

musculature (Figure 2.2) constitutes a complex, dome-shaped arrangement within the pelvic region, akin to a hammock. These muscles are pivotal in upholding continence, facilitating sexual function, and providing support to pelvic organs. Comprising three distinct layers, they intricately interact with the surrounding skeletal structure, fascia, ligaments, and neural networks [20].

The superficial perineal pouch is the first layer that consists of the bulbospongiosus, ischiocavernosus, superficial transverse perineal, and external anal sphincter muscles (Figure 2.3a). This muscle layer plays a significant role in processes such as ejaculation, as well as in maintaining control over urination and bowel movements.

The subsequent layer, termed the urogenital diaphragm, consists of the deep transverse perineal muscles, the sphincter urethrae, and the compressor urethrae. This layer assumes a critical role in ensuring urinary continence, especially during instances of heightened intraabdominal pressure, such as coughing or sneezing [20]. The innermost stratum is the pelvic diaphragm (Figure 2.3b), composed of the following muscles: pubococcygeus, puborectalis, pubourethralis, iliococcygeus, and ischiococcygeus. These muscles play a pivotal role in providing support to pelvic organs and preserving continence [21].

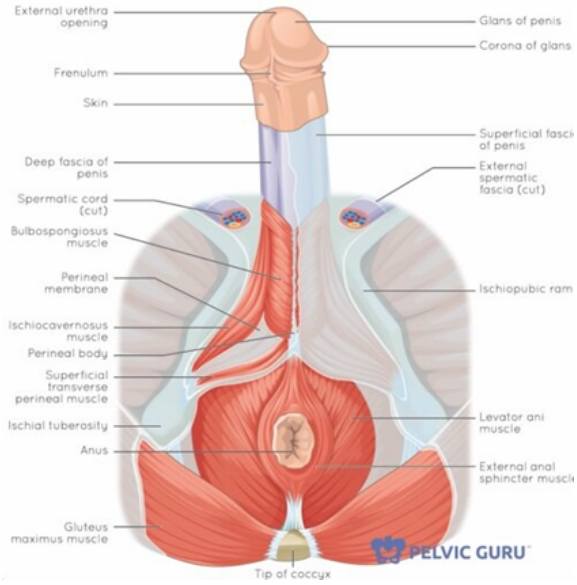

Figure 2.2: Anatomy of the male pelvic foot region, depicting the first layers of muscle.

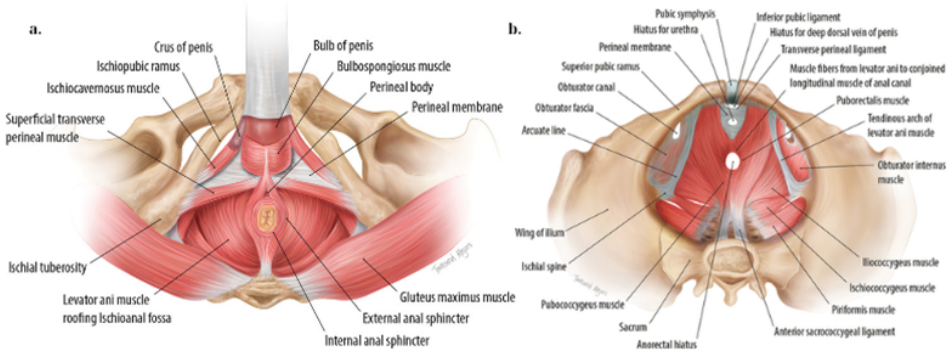

Figure 2.3: Illustration 2.3a illustrates the muscles within the superficial perineal pouch and the urogenital diaphragm, while 2.3b provides a depiction of the muscles located in the deeper layer known as the pelvic diaphragm.

2.2 MRI for the Diagnosis of Male Pelvic Floor Pathologies

In the examination, diagnosis, and treatment planning for male pelvic floor pathologies, MRI imaging emerges as the ideal modality. Male pelvic floor dysfunction encompasses three primary categories: gastrointestinal dysfunction, urinary dysfunction, and sexual dysfunction.

Within the context of gastrointestinal dysfunction, male patients often present with symptoms such as defecatory dysfunction, constipation, or fecal incontinence. These encompass conditions like anorectal junction descent, rectocele, intussusception, rectal prolapse, and transperineal hernias [1]. The role of MRI imaging in understanding and diagnosing these issues is instrumental in ensuring effective care and management for male patients grappling with these disorders.

Male urinary dysfunction encompasses three main symptom categories: lower urinary tract symptoms, functional urinary incontinence, and stress urinary incontinence (SUI). Lower urinary tract symptoms result from issues like poor coordination between bladder muscles and the urethra, leading to irritative voiding symptoms such as urge incontinence and obstructive symptoms like overflow incontinence. Pelvic floor hyperactivity can also contribute to these symptoms [1]. MRI plays a significant role in planning procedures like prostatic artery embolization, classifying benign prostatic hypertrophy, and diagnosing persistent symptoms (Figure 2.4). Functional incontinence, mainly affecting elderly or disabled individuals, stems from limited mobility and is evaluated using imaging to assess complications and exclude other causes of incontinence. Stress urinary incontinence (SUI) is characterized by the leakage of urine during activities that exert pressure on the bladder. This condition is frequently observed in patients who have undergone prostatectomy [1].

Male sexual dysfunction is generally related to hormonal, neurologic, and vascular causes; however, nonrelaxing pelvic floor muscles are thought to contribute to male sexual dysfunction in certain patients, particularly in those with chronic pelvic pain syndrome.

Magnetic Resonance Imaging (MRI) stands as the ideal choice for male pelvic imaging, underpinned by a suite of advantages. First and foremost, its soft tissue resolution enables meticulous scrutiny of the intricate pelvic structures. MRI's inherent non-invasiveness, devoid of ionizing radiation, ensures both patient safety and the viability of longitudinal examinations. Furthermore, its capacity to acquire images

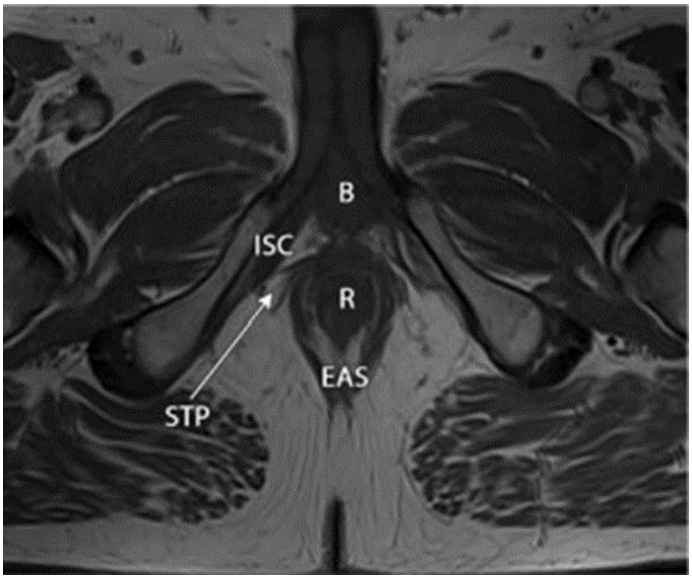

Figure 2.4: MRI image that depicts the region of the lower prostate [1].

across multiple planes empowers clinicians with a comprehensive view of the pelvic anatomy, facilitating precise assessments of intricate structures. Finally, the inclusion of functional imaging techniques, such as diffusion-weighted imaging, bolsters diagnostic capabilities by illuminating tissue characteristics and perfusion, notably enhancing the evaluation of prostate cancer and related pelvic conditions.

CHAPTER 3

FUNDAMENTAL PRINCIPLES OF MRI PHYSICS

In this section, we aim to present a brief overview of the fundamental physics that serves as the basis for MRI scanners. First, we will describe the phenomenon of nuclear magnetic resonance (NMR), delving into its basic principles. Next, our discussion will focus on the T1 and T2 relaxation times, and their correlation with image contrast. In addition, we will provide a brief explanation of the basic MRI sequences that are widely used in clinical settings. This brief overview aims to provide a clear understanding of the fundamental physics integral to MRI scanners, as this knowledge is crucial for the simulation of our computational male pelvic phantom and the image acquisition process.

3.1 Basics of NMR

The signal that detected in clinical MRI is derived from the Nuclear Magnetic Resonance (NMR) phenomenon. Hydrogen nuclei, primarily located within water molecules or bound to fat and protein molecules in tissues, are the sources of the signal. This physical phenomenon is a result of the magnetic dipole moment (μ) exhibited by the protons within hydrogen nuclei and the manner in which these dipole moments react when exposed to an external magnetic field (Ho).

A hydrogen nucleus consists of a single proton, and before delving into the principles of NMR, let's assume that the proton under examination remains unaffected by its electromagnetic environment. In 1964, Murray Gell-Mann and George Zweig proposed the theory that protons are composed of fundamental particles called quarks. Protons, according to this theory, comprise two "up" quarks with a charge of (+2/3)e and one "down" quark with a charge of (-1/3)e, resulting in a net charge of +1e. Simultaneously, these particles exhibit spin, a fundamental property arising from

quantum field theory. The total spin (I) of a proton is +1/2, originating from the spins of its constituent quarks. The proton's peripheral charge and spin give rise to a magnetic dipole moment (μ), which is determined by the equation:

$$\mu = \gamma I \tag{3.1}$$

Here, γ represents the gyromagnetic ratio, a unique property of each nucleus that quantifies the influence of nuclear spin (I) on induced nuclear magnetization (μ) [22]. The gyromagnetic ratio is expressed in units of nuclear Bohr magnetons (μB) times (2π/h), where h is Planck's constant. For a single proton, γ is approximately +2.79*(2πμB/h), and its sign indicates the orientation of μ relative to I (Figure 3.1).

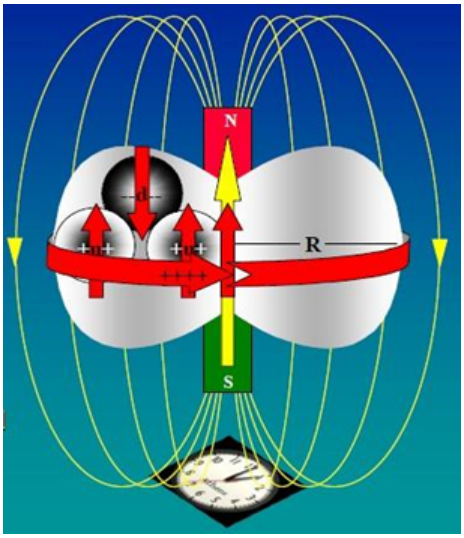

Figure 3.1: In this illustration, the proton is symbolized as a charged sack encapsulating quarks. The yellow arrow signifies the spin (I) of the proton, indicating its orientation and its value derived from the coupling of the quark spins. Being positively charged, the nucleus induces an anticlockwise magnetic rotational motion in the proton, leading to the generation of an induced dipole moment (μ) with an orientation identical to I. The vector representing μ is depicted in red.

The proton, and by extension, the hydrogen nucleus, possesses a randomly oriented permanent magnetic moment in the absence of an external magnetic field. When subjected to a high-intensity external magnetic field (Ho), the randomly oriented magnetic moments (μ) interact with it (Figure 3.2). This interaction follows quantum mechanical laws, leading to two possible orientations of μ with respect to Ho: parallel and anti-parallel, with the most μ aligned parallel to Ho minimizing the energy consumption [23][3].

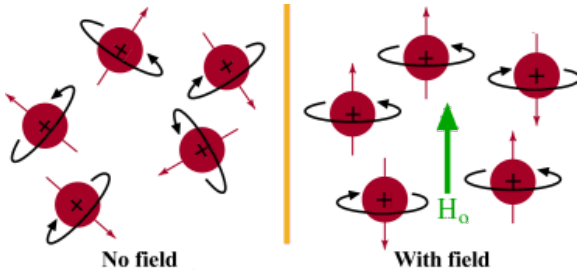

Figure 3.2: The red spheres depict hydrogen nuclei, and the red arrow illustrates the dipole moment (μ). In the absence of an external magnetic field (Ho), the dipole moments of each nucleus exhibit random orientations. However, in the presence of Ho, the dipole moments align in two possible orientations: either parallel or anti-parallel to the applied magnetic field.

Moreover, in an external static magnetic field, the dipole moment (μ) starts to precess. Both μ and I maintain constant magnitudes and vector projections relative to Ho, resulting in "precession"—the rotational motion of the vectors on a conical surface around the chosen axis. On a macroscopic scale, an ensemble of magnetic moments (Mc-isochromats) precesses around Ho at the same angular frequency (ωo) and in phase, forming the volume magnetization (Mo) parallel to Ho (Figure 3.3). The Larmor frequency (ωo) can be calculated using the equation:

$$\omega_0 = \gamma H_0 \tag{3.2}$$

Under these circumstances, if a receiver coil is brought in proximity, no signal will be detected as the net magnetization is stable and remains constant over time. Therefore, to obtain an NMR signal, a change in the magnetic field over time is required (Faraday law), which can be caused by an RF pulse. Nuclear Magnetic Resonance (NMR) is a two-stage resonance process:

A) Excitation session: A radio frequency (RF) pulse is transmitted to the system and the nuclei are subjected to the RF pulse and absorb energy from it.

B) Relaxation session: Nuclei emit energy, which is detected by the receiver coils. The NMR signal is measured during this stage.

3.1.1 Excitation session: Excitation of nuclei within a static homogeneous magnetic field Ho using Radiofrequency radiation (RF).

A specific radio frequency (RF) pulse is applied to the sample, matching the resonance frequency of the nuclei ($\omega_{RF} = \omega_0$). This pulse creates a rotating RF field

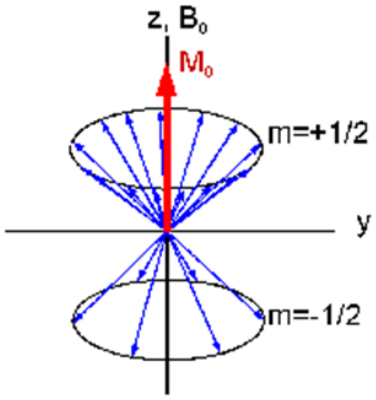

Figure 3.3: The blue arrows represent isochromats (Mc) that are composed of magnetic dipole moments, which precess with same frequency (ωo-larmor frequency) and in phase. This precession is due to the presence of a high-intensity magnetic field Ho, which causes some isochromats to precess parallel to it, while others antiparallel to it. The magnetism Mo arises from the vectorial summation of Mc and is oriented parallel to Ho, as illustrated in the figure. The Bo and the Mo vectors are oriented on the z-axis of the coordination system. Protons at 1 Tesla generate a precessional frequency of 42.6 MHz. This frequency falls within the short radio wave band. [2].

(H1) perpendicular to the static magnetic field (Ho), causing the nuclear magnetization (M) to undergo a precessional motion called "nutation" (Figure 3.4). Nutation refers to any deviation of M from its equilibrium position and includes the motion of isochromats Mc beyond the Larmor precession cone. The angular displacement of M from its initial orientation is quantified by the nutation angle (n), which can be calculated using the equation:

$$n = \gamma \cdot H_1 \cdot t \tag{3.3}$$

Here, γ represents the gyromagnetic ratio, H1 is the RF field strength, and t stands for the duration of the RF pulse.

A crucial concept is the "90-degree RF pulse", which, when applied for a specific duration, causes a complete 90-degree flip of the magnetization vector M, aligning it within the xy-plane. This flip is determined by the magnitude of the nutation angle [3].

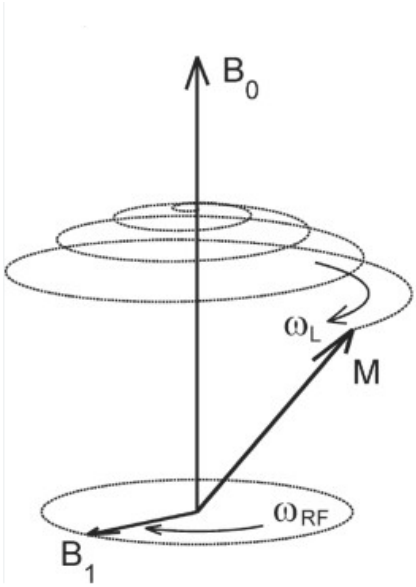

Figure 3.4: The external magnetic field (Bo) aligned along the z-axis, is accompanied by the application of an RF pulse (B1) perpendicular to this field along the x-axis. When the angular frequency of the RF pulse matches the Larmor frequency, the magnetization vector undergoes a nutation motion within the xy-plane. This nutation motion is visually represented by a bold spiral line encircling the z-axis.

3.1.2 Relaxation session: Nuclei inside a homogeneous static external field Ho relaxing to thermal equilibrium.

To facilitate a more concise analysis, we will consider two distinct types of magnetization. Firstly, the longitudinal magnetization Mz, which is developed in the absence of any RF pulse, and the system is under the influence of the magnetic field Ho. Secondly, the transverse magnetization Mxy, which corresponds to the magnetization vector when the RF pulse is applied, causes the magnetization vector to lie within the xy-plane due to excitation. Both the longitudinal and transverse magnetization contribute to the primary magnetization vector M (Figure 3.5).

When the RF pulse is turned off, the transverse magnetization (Mxy) reaches its maximum amplitude, while the longitudinal component (Mz) is reduced to zero. Then, the system gradually returns to its thermal equilibrium state, where the magnitude of the transverse magnetization Mxy decreases, and the longitudinal magnetization Mz increases (Figure 3.6). The whole process is called "magnetic relaxation". Mathematically, the restoration of the transverse magnetization can be described by a decreasing exponential function of time, while the restoration of longitudinal mag-

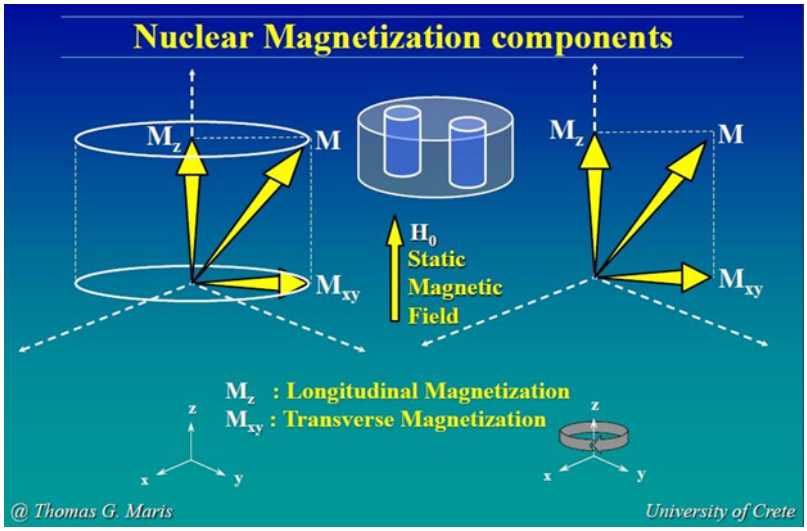

Figure 3.5: The figure illustrates the components of nuclear magnetization (M). The nuclear magnetization consists of two vectors: the longitudinal magnetization (Mz), which is aligned parallel to the static magnetic field (Ho) along the z-axis, and the transverse magnetization vector (Mxy) which is perpendicular to Ho [3].

netization can be described by an increasing exponential function of time, as shown in the above equations:

$$M_{xy}(t) = M_{xy}(0) \exp\left(-\frac{t}{T_2}\right) \tag{3.4}$$

$$M_z(t) = M_z(0)(1 - \exp(-t/T_1)) \tag{3.5}$$

The T1, which is also known as the longitudinal relaxation time, represents the time required for the system to regain 63% of its initial magnetization after being excited by a 90-degree RF pulse. T1 primarily corresponds to the spin-lattice relaxation process, involving the transfer of energy from the excited spins to the molecular framework [3] [6]. On the other hand, T2 is the transverse relaxation time, indicating the timeframe in which 37% of the transverse magnetization is dissipated due to spin-spin interactions. Notably, when the magnitude of Mxy reaches its maximum, it signifies that the isochromats are in phase. However, as the relaxation process progresses, the phase coherence of the isochromats gradually diminishes, leading to a reduction in Mxy.

Above, we presented a mechanism responsible for the reduction of Mxy, based on energy transfer among the spins and the phenomenon of phase coherence, as

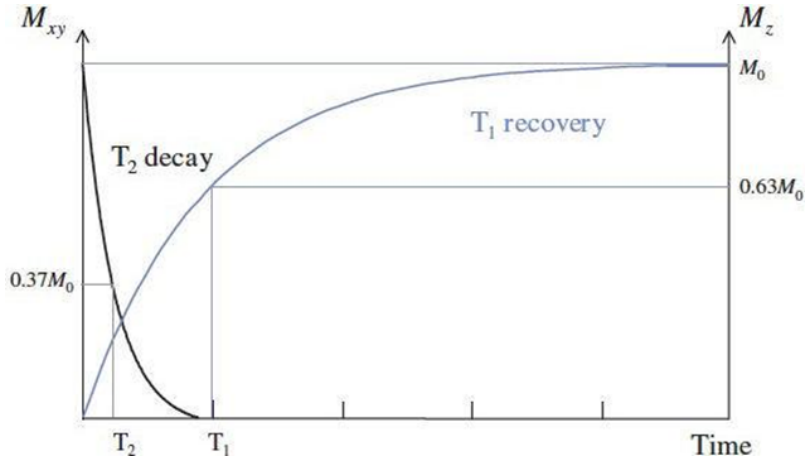

Figure 3.6: This graph illustrates the T1-longitudinal and T2-transverse relaxation times in the context of nuclear magnetic resonance (NMR). The relaxation session commences immediately after the application of a 90-degree radiofrequency (RF) pulse, during which the transverse magnetization (Mxy) reaches its maximal amplitude, and the longitudinal magnetization (Mz) is nearly minimized, approaching zero. The black line represents the exponential decay of transverse magnetization (Mxy). Simultaneously, the longitudinal magnetization (Mz) demonstrates an exponential increase, as illustrated by the blue line. This increase in Mz reflects its gradual restoration over time, as Mxy loses its phase coherence and is minimized [4].

described by T2. There is also a second mechanism attributed to losses due to the non-uniform magnetic field Ho. This scenario also leads to an exponential decrease in Mxy but is characterized by a different time constant, T2'. Therefore, we introduce a new time constant, T2*, which encompasses both T2 and T2', and is expressed by the following relationship [6]:

$$T_2^* = \frac{1}{T_2} + \frac{1}{T_{2'}} \tag{3.6}$$

In this context, 3.6 represents the effective transverse relaxation time, considering the combined effects of T2 and T2' on the decay of transverse magnetization Mxy (Figure 3.7).

The T1 longitudinal relaxation time, the T2 transverse relaxation time, as well as the T2* transverse relaxation time, are intrinsic constants unique to each tissue. These parameters are responsible for the inherent contrast observed in MRI images. Each tissue in the body possesses specific values of these relaxation times, which contribute to the distinct appearance of various anatomical structures in MRI scans. The variations in T1, T2, and T2* relaxation times provide valuable information for differentiating tissues and highlighting specific features in medical imaging, enabling clinicians to make accurate diagnoses and assessments [3] [6].

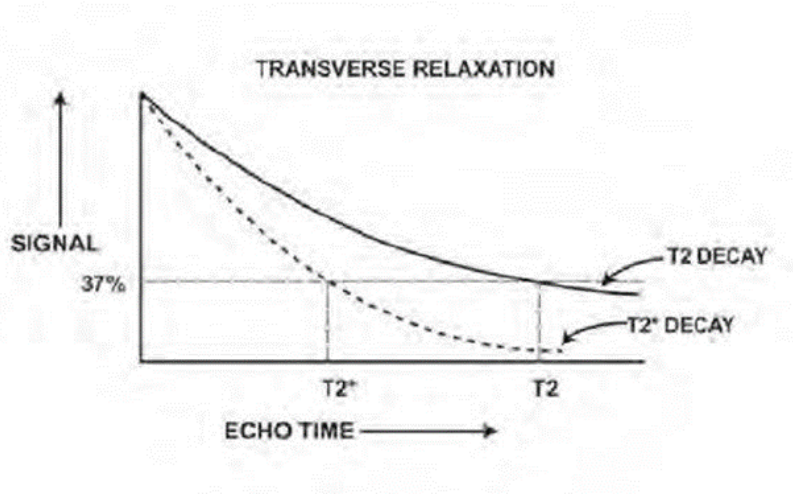

Figure 3.7: In the case of T2 and T2*, the exponential decay of Mxy is depicted. The dashed line represents the exponential reduction of Mxy due to fluctuations in the external magnetic field Ho and spin-spin interactions (T2*). Meanwhile, the solid black line represents the exponential decrease of Mxy solely due to spin-spin interactions (T2). It is evident that in the case of T2*, a more pronounced exponential decay is observed. This is entirely logical considering that there are additional factors contributing to the loss of phase coherence in the system. Hence, the T2* time constant is smaller than T2, reflecting the faster rate of decay due to the combined effects of external field variations and spin-spin interactions [5].

3.2 Contrast in MRI: T1, T2, T2*

The parameters T1, T2, and T2* have main importance in MRI, as they are responsible for the inherent contrast among various tissues in MRI. As stated earlier, T1, T2, and T2* are time constants with unique values for each tissue type. Based on the desired tissue contrast, MRI images are categorized as T1-weighted, T2-weighted, or proton density (PD)-weighted images. The selection of the appropriate imaging category plays a pivotal role in accurate diagnosis and effective treatment planning, as each category provides unique insights into tissue characteristics.

Before progressing further, it is important to highlight that the generation of MRI images involves the application of specific sequences. These sequences play a fundamental role in determining the timing for signal acquisition and the precise moments at which subsequent radiofrequency (RF) pulses are applied. Two principal families of sequences are commonly employed, known as Spin Echo (SE) and Gradient Echo (GRE). The sequence of SE will be thoroughly examined in the next subsection. At this moment, it is pertinent to note that each sequence is distinguished by two crucial parameters: the Echo Time (TE) and the Repetition Time

(TR). The TE designates the temporal interval between the application of the 90-degree RF pulse and the moment of signal acquisition. On the other hand, the TR denotes the duration between successive 90-degree RF pulses during the sequence. By appropriately adjusting these TE and TR parameters, MRI systems can produce images with varying tissue contrasts and capture specific anatomical features.

3.2.1 T1-weighted image

A T1-weighted (T1w) image serves to highlight variations in signal intensity due to the inherent T1 relaxation times of different tissues. These images are especially valuable in clinical practice for visualizing normal anatomy, identifying lesions, and highlighting tissue boundaries. T1w imaging is widely employed in diagnosing brain, spine, and musculoskeletal conditions, as well as for examining abdominal and pelvic organs.

Consider that there are three distinct tissues, each possessing different T1 values as illustrated in Figure 3.8. In a T1-weighted image, the tissue with a lower T1 value appears bright, while the tissue with a higher T1 value appears dark. This phenomenon happens because, when we capture the signal within a time interval smaller than the lower T1 value, the tissue with the shorter T1 accumulates a higher Mz magnitude, leading to the detection of a stronger signal from that specific tissue [6]. As a general guideline in T1-weighted imaging, we can anticipate that tissues with short T1 values will appear brighter, while tissues with longer T1 values will appear darker. The contrast of the T1-weighted image is modulated by the careful selection of TE and TR.

T1 Contrast

The TE and TR parameters influence the contrast in T1-weighted images. In an MRI sequence, we apply a series of RF pulses, and the duration between two consecutive RF pulses is referred to as the repetition time (TR). The signal is then detected at a specific time interval after the application of the RF pulse, known as the echo time (TE). Both the TR and TE parameters are adjusted by the MRI operator. To create a T1-weighted image, we require both a short TE and a short TR.

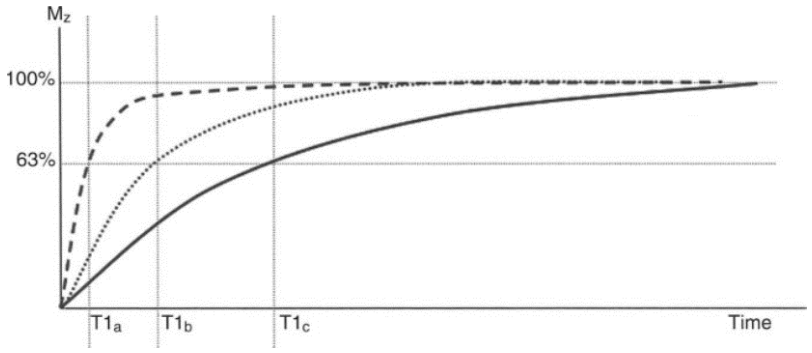

Figure 3.8: In this illustration is depicted the diagram of the longitudinal relaxation of three different tissues. The T1 signifies the duration it takes for 63% of the initial magnetization to recover. Each line corresponds to different tissue: the dashed line symbolizes fat, characterized by a short T1 (T1a); the solid line depicts CSF, with an extended T1 (T1c); and the dotted line represents brain tissue, featuring an intermediate T1 (T1b). In a T1-weighted image, fat appears brighter, brain tissue is displayed in shades of gray, and CSF appears darker. To notice that the image's contrast is influenced by the suitable selection of TE and TR, which are determined by the MRI operator [6].

3.2.2 T2-weighted image

The T2-weighted (T2w) image highlights variations in the T2 relaxation time among different tissues. Clinically, T2-weighted images offer the most effective visualization of diseases due to the elevated water content that is typically found in tissues affected by pathological processes. Regions with increased water content, such as those containing fluids like cerebrospinal fluid and vitreous humor, appear illuminated on T2-weighted images [24].

Visualize a situation in which there are three distinct tissues, each characterized by its own distinct T2 values, as depicted in Figure 3.9. The time constant T2 represents the duration it takes for 63% of the magnetization to decay. During the relaxation process, the transverse magnetization vector Mxy experiences an exponential decrease. In T2-weighted imaging, tissues with long T2 values appear bright, while tissues with shorter T2 values appear darker. This occurs because, in tissues with shorter T2 values, the signal weakens more rapidly compared to tissues with longer T2 values. As a result, we receive a weaker signal from tissues with short T2 and a stronger signal from tissues with long T2 values [6].. Just to remind you the signal is collected during the relaxation process. So, in Figure 3.9, if the signal is detected in TE: $T_{2b} < \text{TE} < T_{2c}$, then "c" tissue will appear brighter, "b" tissue will appear as a mid-tone in grayscale, and "a" tissue will appear darker.

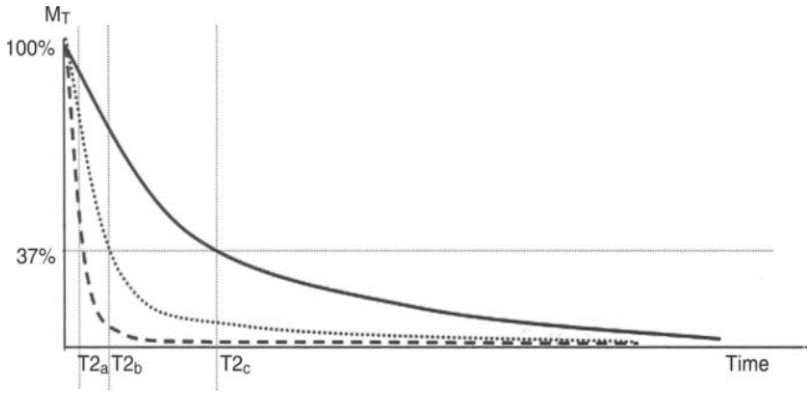

Figure 3.9: In this illustration is depicted the diagram of the transverse relaxation of three different tissues. The T2 represents the duration it takes for 63% of the magnetization to decay. Each line corresponds to different tissue: the dashed line symbolizes fat, characterized by a long T2 (T2a); the solid line depicts CSF, with a long T2 (T2c); and the dotted line represents brain tissue, featuring an intermediate T2 (T2b). In a T2-weighted image, fat appears darker, brain tissue is displayed in shades of gray, and CSF appears bright [6].

T2 Contrast

T2-weighted images are generated using long TE and long TR. In the context of the two-tissue example, let's assume that we've applied a 90-degree RF pulse, resulting in the maximum magnitude of transverse magnetization (Mxy). To establish T2-based contrast, it becomes essential to acquire the signal at a long echo time (TE). This is crucial because, at the outset, all tissues possess identical magnetization magnitudes ($Mxy_a = Mxy_b = M_0$). Moreover, it's essential to utilize a long repetition time (TR) to ensure that the magnetization of each tissue has ample time to reach its maximum transverse magnetization magnitude. During the relaxation process, tissues with shorter T2 values experience a more rapid decrease in their magnetization compared to tissues with longer T2 values. This variance enables us to discern and differentiate between the tissues effectively.

3.2.3 PD-weighted

Utilizing the distinct proton density inherent to each tissue, we can create images that leverage this property, known as proton density (PD)-weighted imaging. To achieve PD-weighted images, it's essential to minimize the influence of tissue T1 and T2 contrasts. This is accomplished by employing long TR to diminish T1 contrast and short TE to reduce T2 contrast [6]. This careful calibration ensures that the resulting images primarily highlight proton density differences among tissues, offering

valuable insights into tissue composition and aiding in clinical diagnoses.

More specifically, each tissue possesses a distinct proton density, meaning that a specific number of protons corresponds to a voxel within the tissue. As the signal originates from the protons of hydrogen nuclei, tissues with higher proton density will generate a larger magnetization vector. Consequently, in PD-weighted imaging, they will appear brighter. Conversely, tissues with lower proton density result in a smaller amplitude of the magnetization vector (Mo) and are represented as darker areas.

3.3 MRI Sequences

The MRI sequences are employed instead of direct signal detection due to their pivotal role in optimizing image quality, contrast, and sensitivity. A pulse sequence, essentially a "sequence of events," involves handling RF pulses, gradient fields, and signal collection in the context of MRI. In this section, we'll explore MRI sequences by focusing more on the spin-echo (SE) sequence. By carefully choosing the appropriate values for TE (echo time) and TR (repetition time) in each sequence, it is possible to generate T1-weighted, T2-weighted, and PD-weighted images. Furthermore, sequences offer the advantage of managing artifacts and contrast suppression, enabling the production of images with clinical significance.

3.3.1 Spin Echo (SE)

Clinically, the applications of SE sequence underscore its importance in medical imaging. From neuroimaging to musculoskeletal and abdominal studies, SE sequences find utility in diverse clinical scenarios. Their adaptability to different anatomical regions, coupled with the capacity for multiplanar imaging, facilitates comprehensive assessments of structures throughout the body. The principal advantage of the Spin-Echo (SE) pulse sequence lies in its ability to mitigate signal losses arising from external field inhomogeneities.

The spin echo sequence is designed to restore the lost transverse magnetization vector (Mxy) resulting from external magnetic field variations, effectively countering the impact of T2* effects. In environments with magnetic field heterogeneity, spins experience diverse magnetic fields (Ho) and undergo precession at distinct Larmor frequencies (ωo). This variation in spin behavior results in a rapid loss of phase co-

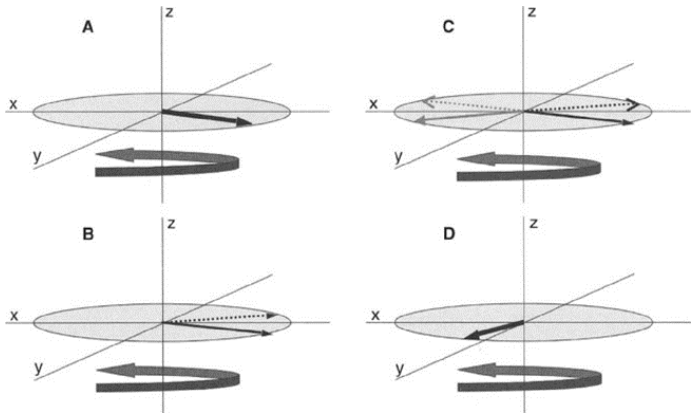

Figure 3.10: The physics underlying the Spin Echo sequence: A) The transverse magnetization vector (Mxy) in xy-plane, resulting from the 90-degree RF excitation pulse. B) Due to variations in the external magnetic field (Ho), the amplitude of Mxy decreases due to loss of phase coherence. The dotted arrow is positioned ahead of the solid arrow. C) A 180-degree RF pulse is administered, leading to a reversal in the phase of the spins. Consequently, the dotted arrow moves behind the solid arrow. D) As a result of this phase reversal, the spins come back into phase, maximizing the amplitude of the transverse magnetization vector. At this point, the signal is detected by the receiver. The signal is detected at TE and the 180-degree RF pulse is applied at TE/2. [6].

herence over time, as some spins accelerate more quickly than others (Figure 3.10B). To address this challenge, the spin echo sequence operates on the principle of phase inversion for the spins, by applying a 180-degree refocusing pulse (Figure 3.10C). By flipping the phase, the rapidly precessing spins synchronize with the slower precessing spins, restoring phase coherence (Figure 3.10D), and at this moment the signal is collected. It is important to note that the phase inversion must occur midway between the initial RF pulse and the TE at TE/2.

So, the incorporation of a 180-degree refocusing pulse within the SE sequence enhances image sharpness and clarity, rendering it a favored option in diverse clinical applications where the precision of image quality is imperative for accurate diagnostic evaluations. Furthermore, SE sequences provide high tissue contrast, allowing for clear differentiation between different types of soft tissues. This is crucial for visualizing anatomical structures and detecting abnormalities. While the SE sequence presents advantages such as clear tissue contrast and resilience against motion artifacts, its drawback lies in the extended time required to complete a scan.

3.3.2 Gradient Echo (GRE)

The Gradient Echo (GRE) sequence is a crucial component of clinical MRI, especially in contexts where rapid image acquisition is essential, such as cardiac MRI and

contrast-enhanced MR angiography. Its key advantage lies in the use of a short repetition time (TR) combined with a variable low flip angle. This specific configuration is designed for fast imaging applications, ensuring swift data acquisition.

GRE sequences find applications in various clinical scenarios, including cardiac imaging, musculoskeletal imaging, and angiography, showcasing their versatility in different medical contexts. The rapid imaging capabilities of GRE sequence make them suitable for functional MRI studies and sensitive to flow-related effects, making them useful in angiography and dynamic contrast-enhanced imaging. In the Gradient Echo (GRE) sequence, the lack of a 180-degree pulse results in signal losses attributed to T2* effects. Consequently, the total signal sampled during a GRE pulse sequence is lower compared to a Spin Echo (SE) pulse sequence.

CHAPTER 4

DESIGNING OF COMPUTATIONAL MALE PELVIS PHANTOM

In this chapter we will present the process that followed to create our computational human phantom, starting from a dataset of MRI images of the male pelvis and ending up with a computational phantom that accurately depicts its geometry and mimics the properties of real tissues.

4.1 Designing Process of Phantom

At the beginning of our project, we aimed to create a phantom emulating the imaging MRI parameters pertinent to the constituent tissues of the male pelvis. Specifically, our focus centered on mirroring the characteristics of fat and muscle within a male pelvic phantom, as these constitute the primary components. The essential MRI parameters encompassed the T1 transverse relaxation time, T2 longitudinal relaxation time, and PD (proton density) for each tissue. These values, integral to the relaxometry process in clinical MRI, were meticulously extracted from relevant literature [25].

Given the nascent stage of our investigation and the uncertainty surrounding the representation of pelvic anatomy in our virtual phantom, we decided to use simple geometric shapes and encapsulate the corresponding tissue MRI parameters (Figure 4.1). This process proved to be straightforward, facilitated by the simulation platform's inherent provision of predefined geometries. By utilizing the simulation platform (Chapter6) and working with basic geometric shapes, we engaged in a hands-on educational experience of MRI simulation platform and the scanning process for the image acquisition (Figure 4.2). Acquiring virtual MRI images isn't straightforward—it requires a solid grasp of magnet physics and training in applying sequences to achieve the desired image contrast.

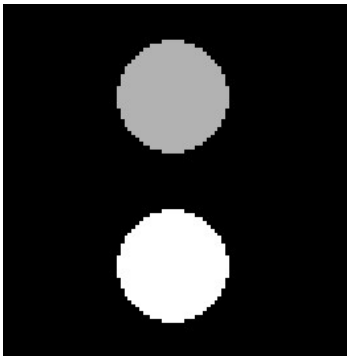

Figure 4.1: Virtual phantom spheres showcasing MRI properties of muscle and fat. Created in the MRiLab simulation platform, these spheres were used for training in MRI simulation scanning. The upper sphere symbolizes muscle, while the lower one represents fat tissue. The image contrast is determined by proton density, with the values presented in Table 4.1

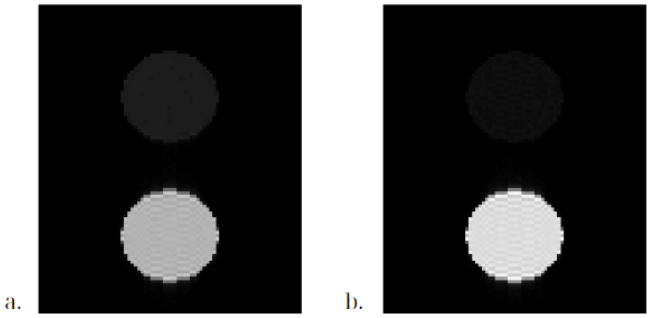

Figure 4.2: MRI images of the phantom acquired using the SE sequence. a) T1-weighted image obtained with TE=20ms, TR=450ms and flip angle= 90 degrees. b) T2-weighted image with TE=90ms, TR=3500ms and flip angle= 90 degrees.

The objective of this thesis is to develop a computational male pelvic phantom that faithfully replicates the anatomical structures and associated tissue properties of the human body, departing from simplistic geometric forms. Emphasizing the representation of authentic tissue anatomy in our virtual phantom is crucial, given the impact of geometry on imaging, resolution, and contrast in medical images.

In pursuit of our computational phantom design objective, we exploit the Constructive Solid Geometry (CSG) modeling approach as discussed in Chapter 1. So, for the reconstruction of the male pelvis phantom, we leveraged the advantages of tomographic technologies, specifically magnetic resonance imaging (MRI), in tandem with advanced image processing techniques. This approach enabled the creation of a highly precise and detailed pelvis phantom for MRI simulation processes. Our

dataset was composed of 22 MRI slices of 512x512 pixels, depicting the male pelvis region of a patient. As you can see, in Figure 4.3 is depicted a 2D image of 512x512 pixels of our 22 slices dataset. The images were provided to us by the General University Hospital of Heraklion.

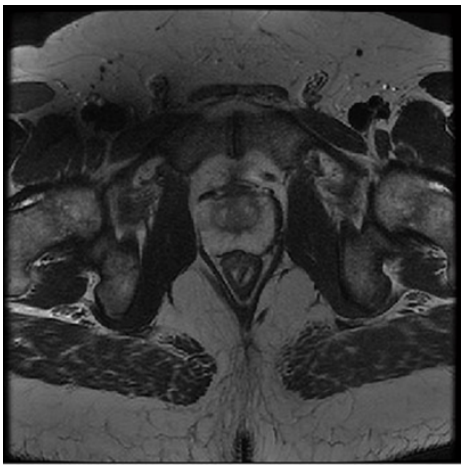

Figure 4.3: Clinical MRI image of man's pelvis. It is depicted a single slice of 512x512 pixels from our dataset of 22 slices. The images were provided to us by the General University Hospital of Heraklion.

Our initial step involved segmenting the acquired images into distinct anatomical regions of interest. For the male pelvis, these regions included fat and muscle. The segmentation was through the Mango software tool [26], which is designed to facilitate image analysis tasks. The segmentation process involved finding the respective tissue from the histogram of the main image, isolating the tissue, and saving it in binary format. In the binary image format, regions of interest were assigned the value of 1, while non-interest regions were assigned the value of 0, as depicted in Figure 4.4. For instance, the fat mask assigned a value of 1 to each pixel representing fat tissue and a value of 0 to every pixel corresponding to muscle tissue. This process resulted in the creation of two binary mask datasets: one containing only muscle and the other containing solely fat. The binary masks have the same resolution as the main MRI image (512x512 pixels).

After creating our binary masks, we proceeded to our main MRI dataset and applied each mask separately for each tissue, i.e., we masked our main MRI dataset for fat and muscle. We multiplied the pixels of the main MRI image with the corresponding pixels of the mask. Pixels in the main MRI image that were multiplied by 0 were set to zero, while those multiplied by 1 retained their original tissue intensity values. As a result, the two masked datasets were three-dimensional (3D) with di-

Figure 4.4: This figure illustrates the two 2D binary images of fat (left) and muscle (right) that were used for the reconstruction of the male pelvic phantom. Both mask images have a resolution of 512x512 pixels, as the initial MRI image of Figure 4.3. In binary format images, the value 1 is represented in white, while 0 is depicted in black.

mensions of 512x512x22 pixels, with one dataset exclusively representing muscle and the other solely representing fat.

Subsequently, we had to assign tissue properties to each dataset. As mentioned in a previous section of the thesis, each tissue type possesses distinct parameters, and consequently, each tissue yields a different NMR signal. The parameters influencing the signal of each tissue include T1, T2, T2*, proton density, and mass density. The concept was to mimic each tissue by assigning the respective parameter values based on the literature [25]as shown in Table 4.1.

Tissue Type	**T1 (ms)**	**T2 (ms)**	**T2* (ms)**	**Proton Density**	**Mass Density (kg/m^3)**
Muscle	1.420	0.0317	0.015	0.7	1090
Fat	0.365	0.133	0.05	1	911

Table 4.1: This table presents the tissues of the male pelvis along with their corresponding MRI parameter values, sourced from the literature [25].

To assign values to each tissue, we worked on each masked image dataset separately. For instance, in the dataset exclusively representing muscle tissue, we generated five separate matrices, each corresponding to a specific parameter. In these matrices, we replaced the values that weren't zero (indicating tissue) with the respective parameter value. For example, in the T1 matrix for muscle tissue, where the pixel value wasn't zero, we substituted it with 1.1, and so on (Table 4.1). Each of these parameter matrices is also sized at 512x512x22 pixels.

To create the complete male pelvic phantom, we amalgamated the distinct parameter matrices associated with each tissue type into a comprehensive dataset,

creating a virtual object. This process was executed through MATLAB 13 scripts. Within these scripts, we instantiated an object representing the final phantom, with the integrated parameter matrices serving as its inherent properties. In Figure 4.5 on the left side, a 2D representation of the final male pelvic phantom is depicted, showcasing induced parameters in both fat and muscle. The ultimate phantom possesses dimensions of 512x512x22, some of the corresponding slices are illustrated at the right side of Figure 4.5.

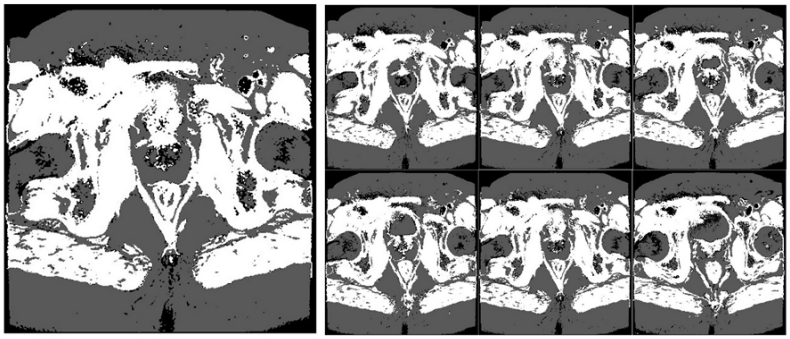

Figure 4.5: On the left side, we have a 2D representation of the completed male pelvic phantom. This image is presented in grayscale, with varying shades of gray corresponding to different values of the T1 parameter. The image is displayed at a resolution of 512x512 pixels, providing a detailed view of the phantom's composition. Moving to the right, we are presented with a visual depiction of six individual slices extracted from the 3D representation of the final phantom. These slices are part of a set of 22 total slices that provide a comprehensive and detailed view of the entire 3D phantom.

Through tomography and basic image processing techniques, we've successfully generated a virtual male pelvic phantom. This model faithfully reproduces the anatomy of real tissues and accurately integrates their specific properties. It now serves as a standard for examining MRI sequence protocols and acquiring image datasets. At this point, we would like to summarize the process of reconstructing and designing the male pelvic phantom. The steps involved in creating this phantom can be outlined as follows 4.6:

1. **Dataset Acquisition:** The first crucial step involved obtaining a dataset that focused on the specific anatomic region of interest, which, in this study, depicted the male pelvic region.

2. **Tissue Segmentation:** Subsequently, the acquired dataset underwent segmentation to delineate the tissue anatomy, resulting in the creation of binary tissue masks.

3. **Masked Dataset:** The original image dataset was then systematically masked using each tissue mask separately. This process yielded two distinct masked datasets.

4. **Tissue Parameter Incorporation:** Tissue-specific parameters, such as T1, T2, T2*, Proton Density, and Mass Density, were introduced into the masked datasets based on relevant literature. This step led to the creation of five matrices for each masked dataset, one for each tissue parameter.

5. **Final 3D Phantom Creation:** The culmination of this effort was the development of a 3D male pelvic phantom. This was achieved by creating a dedicated virtual object and defining it with the tissue parameter matrices. The resulting 3D male pelvic phantom possessed dimensions of 512x512x22 pixels, and for each tissue parameter, five corresponding 512x512x22 matrices were established.

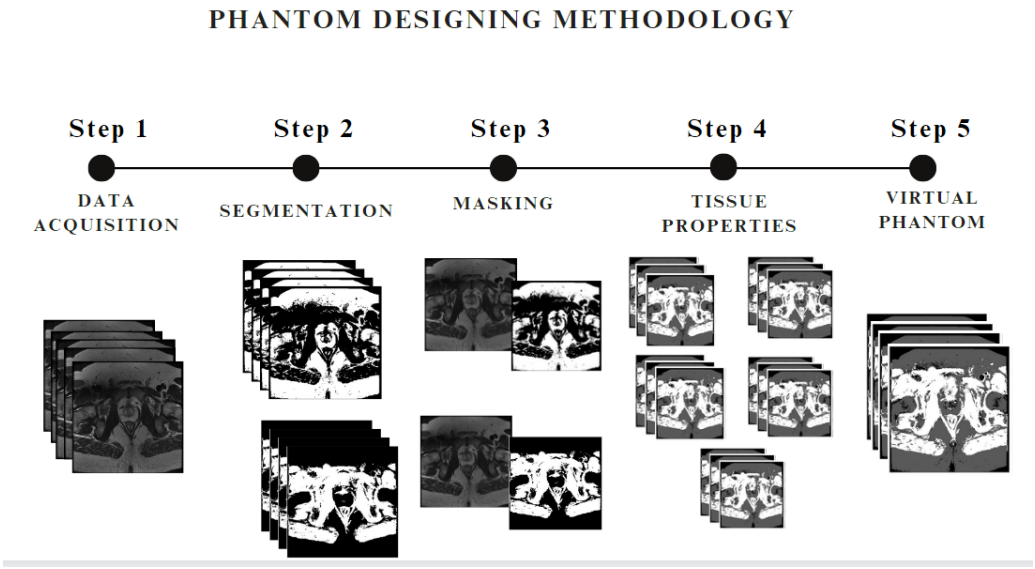

Figure 4.6: This image provides a concise summary of the procedures undertaken to construct the computational male pelvis phantom. Basic image processing techniques, such as segmentation and masking were applied to achieve our final target. Each step is accompanied by the corresponding datasets utilized in the process, giving a better representation of the phantom designing process. The values of the tissue properties are included in Table 4.1

CHAPTER 5

MRI SIMULATOR

In this fifth chapter, we introduce the simulation platform employed for obtaining MRI images of the computational male pelvic phantom. Additionally, we delineate the capabilities and functionalities of the simulator, along with detailing the methodology employed throughout the scanning process.

5.1 MRiLab Simulator

Our experimental work was conducted using MRiLab, an open-source MRI simulation software developed by Fang Liu, which is readily accessible online [27]. MRiLab serves as a comprehensive software suite for simulating various aspects of MRI procedures, including signal generation and image reconstruction. It provides a wide array of tools for designing MRI sequences, investigating magnetic field characteristics, and facilitating the development and evaluation of novel MRI techniques and applications.

Since the early 2000s, several open-access MRI simulation platforms have been developed, such as SIMRI [28] and Virtual MRI [29]. These platforms have been utilized for educational purposes and to familiarize students and trainees with the operation of MRI scanners. A significant limitation of these MRI simulators was their reliance on simplified tissue representations, where all protons are assumed to reside in a single compartment, rather than adopting a more realistic biological model where protons interact within multiple compartments. This limitation leads to incomplete descriptions of MRI signal and tissue contrast. Consequently, integrating more complex tissue models that account for multiple exchanging proton pools is imperative to overcome this limitation and achieve precise tissue representation. The MRiLab has these capabilities, as incorporates a multi-pool description of spin inter-

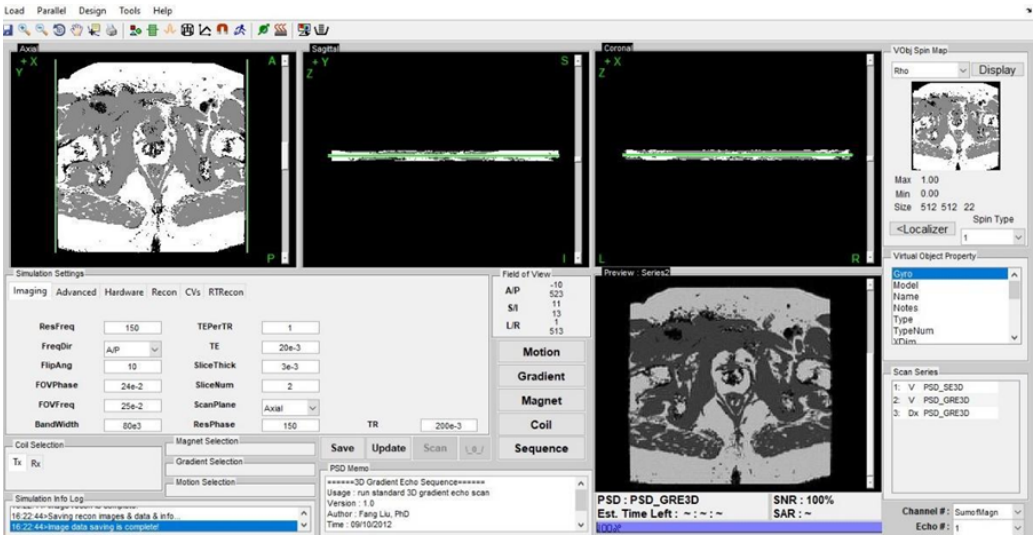

Figure 5.1: The MRiLab simulator console. In the upper right corner, there's a miniature representation of the imaging phantom that was uploaded to the simulator. This phantom serves as the basis for generating our MRI image. In the lower right corner, there's the actual image displayed.

actions, characterizing better the tissue composition, and microstructure, surpassing mere pathology visualization.

In the MRiLab, the signal generation process entails solving the Bloch equations individually for each voxel in our image. Through this process, the k-space is created, and applying FFT reconstruction algorithms the final MRI image is generated. The MRiLab simulation tool, along with its complete set of functions, is designed for compatibility with ≪MATLAB 13≫ and offers the capability for accelerated calculations through GPU utilization. Figure 5.1 depicts the MRiLab simulation platform, notable for its striking resemblance to the console of a magnetic resonance imaging modality.

Our selection of MRiLab as our primary simulation tool was driven by several key factors. Firstly, it excels in providing a robust mathematical representation that closely approximates real MRI scanners. This capability is underlined by its continuous evolution in modeling spin interactions and its consistent alignment with experimental results, as evidenced by prior research [30]. Moreover, its recognition and acceptance within the international conference circuit bolster its credibility. Additionally, the open-source nature of MRiLab and its implementation in a user-friendly language like Matlab played a pivotal role in our decision.

5.2 Simulation Process

To efficiently conduct a magnetic resonance imaging simulation, the initial step involves the upload of our computational phantom. Concerning computational phantoms, the platform offers pre-constructed phantoms designed to mimic human tissues. These readily available phantoms serve as valuable resources for users to familiarize themselves with the platform's functionalities. Moreover, the platform facilitates the creation of custom phantoms, constraining users to specific geometric shapes such as spheres, pyramids, etc. Additionally, it extends the capability to upload user-generated imaging phantoms in the mat file format. In our experiments, we employed a custom-designed 3D computational phantom specifically tailored to replicate the male pelvic region, accurately capturing both muscle and fat regions. This phantom had dimensions of 512x512x22. Chapter 4 provides a comprehensive reference for all the stages involved in the design of the male pelvic phantom.

Upon uploading the computational phantom, the subsequent step involves selecting the desired scanning sequence. MRiLab offers a comprehensive range of fundamental sequences, including Spin Echo (SE), Gradient Echo (GRE), and Inversion Recovery (IR) that are used in clinical practice. Furthermore, MRiLab provides users with the flexibility to experiment with and even create their unique sequences using the sequence design panel. Consequently, MRiLab proves to be an invaluable tool for both generating MRI sequences and facilitating user experimentation and exploration of MRI sequence design.

Once the scanning sequence is chosen, we can directly modify imaging settings from the console. This enables us to tailor image parameters to our specific requirements, as exemplified in Figure 5.1. These parameters encompass various aspects of the image, including TE (Echo Time), TR (Repetition Time), resolution along the frequency/phase axis, tissue slice thickness, flip angle, and field of view (FOV) along the frequency/phase axis. It's important to mention that, in addition to imaging parameters, the simulator incorporates settings related to the selection of the external magnetic field, noise levels, and more. The scanning process initiates after the suitable MR sequences and scanning parameters have been chosen.

In general, the acquisition time for an image in a real MRI scanner is calculated using the above formula:

$$\text{Total Imaging Time} = \text{TR} \cdot \text{Np} \cdot \text{NEX} \tag{5.1}$$

In equation 5.1, TR is the time between two successive pulses in a sequence, Np is the number of phase encoding steps and NEX represents the number of excitations, which indicates how many times the same image is acquired and averaged to enhance the final image's quality.

The average time of an MRI scan is 30 to 60 minutes, the MRiLab simulator doesn't offer realistic imaging times for image acquisition. For instance, the average scan time for a T2-weighted SE sequence with TR=3500, Np=150, and NEX=3 is approximately 1 hour and 20 minutes. Similarly, for a T2-star-weighted GRE sequence with TR=400, Np=150, and NEX=3, it's around 50 minutes. The above time intervals concern the acquisition of two male pelvic phantom slices. Moreover, by increasing the Np from 150 to 256 the imaging time for the above T2-weighted SE increased to 2 hours and 45 minutes. When a GPU is employed for parallel processing, these acquisition times can become even more efficient and approximate those of real MRI modalities.

After acquiring the MRI image, MRiLab offers a range of image processing capabilities, such as creating regions of interest (ROIs), calculating image statistics for both ROIs and the entire image, applying various filters, and assessing their effects on the image, among other functions. In our approach, we choose to develop custom scripts in Matlab for in-depth image analysis.

5.3 Additional Interesting Functionalities of MRiLab

A valuable capability of MRiLab is the simulation of patient motion. Motion introduces unwanted noise into the resulting MR images, and MRiLab allows users to simulate and analyze these scenarios, aiding in a deeper understanding of motion's impact on image quality. Furthermore, within the magnet and RF designing panels, users possess the capability to design gradient magnetic fields, and RF pulses, and account for inhomogeneities in external magnetic fields, tailoring these elements to their specific requirements and experimental objectives. For example, they can investigate artifacts stemming from the selection of these technical parameters, such as the zipper artifact caused by RF inhomogeneities. Moreover, they can examine MRI machine variability by simulating different MRI protocols.

An additional, particularly engaging function, geared mainly toward educational

purposes and enhancing understanding of the fundamental principles of magnetic resonance imaging, is the "SpinWatcher" feature. This feature is specifically designed to depict in the form of a diagram the changes in the magnetization vector and its components, Mxy and Mz, within a designated voxel, all under the influence of user-defined MR sequences and field conditions.

5.4 Advantages of MRiLab

An advantage of the MRiLab simulator in relation to similar software simulators is its ability to represent tissue micro-structure by adopting a generalized tissue model. This generalized model incorporates multiple interchanging water and macromolecular proton pools, instead of relying on a system of independent proton isochromats as commonly used in earlier simulation tools. These approaches encompass various techniques, including quantitative magnetization transfer (qMTI), multi-component spin-lattice (T1) and spin-spin (T2) relaxometry, as well as chemical-exchange saturation-transfer (CEST) methods. In this study, we did not utilize the capabilities of bounded pools; instead, we focused on free pool tissues. Bounded pools represent our future work direction for upcoming research.

One limitation observed during the utilization of the MRiLab simulator is that the software imposes certain parameter value limits, preventing the exploration of extreme values. While this restriction is not necessarily detrimental, as it is designed to produce results applicable in clinical contexts, it may pose constraints in the research domain where greater flexibility is desired.

CHAPTER 6

PHANTOM MRI SCANS

In this chapter, we present MRI images obtained by scanning the male pelvis phantom using a fundamental MRI sequence. We utilized the SE sequence, resulting in images featuring T1-weighted (T1w), T2-weighted (T2w), and proton density (PD) contrasts. The acquisition of MRI images wasn't a simple process, as it required the study of the physics governing the MRI sequences and finding the appropriate values of the TE/TR parameters to obtain the desired contrast that coincided with the clinical protocols.

Throughout our experiments, we conducted scans within an external magnetic field of 3 Tesla (3T). In all of the MRI images, we selected the same Field of View (FOV). The choice of the appropriate FOV has particular significance in medical imaging as it is closely related to image resolution and Signal-to-Noise Ratio (SNR). To create the following images, we utilized an FOV of 24 cm in the phase-encoding and 25 cm in the frequency-encoding direction.

6.1 Spin Echo Images

In our study, we generated T1-weighted (T1w) and T2-weighted (T2w) contrast images of our computational human phantom using a Spin Echo (SE) sequence. As discussed in Chapter 3, acquiring T1w contrast is accentuated by short Echo Time(TE) and short Repetition Time (TR), while creating T2w contrast calls for a long TE and TR duration. For the Proton Density (PD) image, it is crucial to suppress both T1 and T2 influences. Therefore, it suffices to approximate the initial FID amplitude by choosing a short TE and a long TR to derive a PD image. Furthermore, it's important to note that T1 contrast depends on modifications in TR, and T2 contrast is contingent on modifications in TE.

The scanning parameter values utilized in our experiments are summarized in Table 6.1 below.

Scanning Parameters	SE-T1w	SE-T2w	SE-PDw
TE (ms)	20	90	10
TR (ms)	450	3500	3500
RF flip angle (degree)	90	90	90
Slice Thickness (mm)	3	3	3
Slice Num	2	2	2

Table 6.1: This table outlines the scanning parameters employed for the generation of images featuring three distinct contrasts (T1w, T2w, and PDw) utilizing the SE sequence. It includes key characteristics such as TE and TR times, the examined slice thickness, the RF excitation flip angle, and the parameter 'Slice Num' denoting the number of the imaging slice.

SE Scanning Images

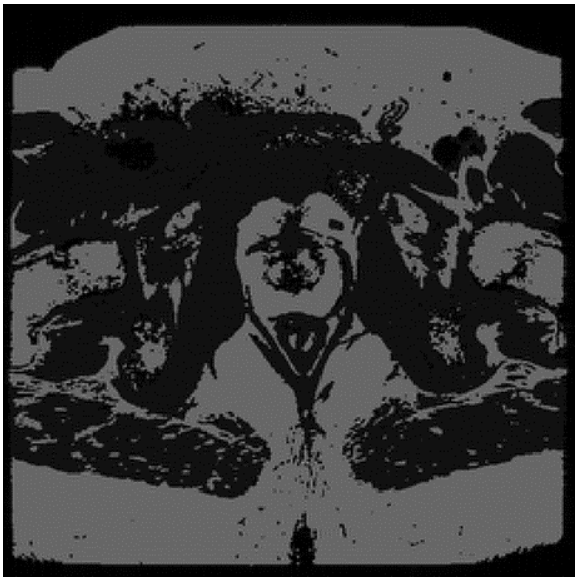

Figure 6.1: SE-T1w Image (TE=20ms, TR=450ms and flip angle=90-degree) of the male pelvic phantom showcasing enhanced brightness in fat regions owing to its lower T1 value. The grayscale image is presented in a 256x256x2 format, and a 2D representation is illustrated here.

In the SE-T1w image (Figure 6.1), fat appears with brighter intensity compared to muscle tissue. This result aligns with expectations, given that T1w images typically portray tissues with lower T1 values as brighter than those with higher T1 values.

This correlation is further illustrated in Table 6.1, highlighting the lower T1 value of fat in comparison to muscle.

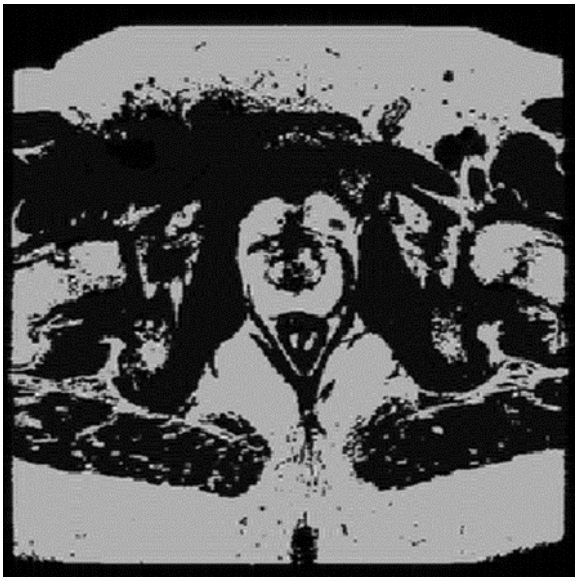

Figure 6.2: SE-T2w Image (TE=90ms, TR=3500ms and flip angle=90 degree) of the male pelvic phantom. Fat appears brighter than muscle due to its higher T2 value compared to muscle tissue (Table 6.1). The grayscale image is presented in a 256x256x2 format, and a 2D representation is illustrated here.

In the SE-T2w image (Figure 6.2), fat is depicted with greater brightness compared to the muscle tissue. This observation was in line with our expectations, as T2w images typically render tissues with higher T2 values as brighter in contrast to those with lower T2 values. Additionally, a reference to Table 6.1 reveals that fat possesses a higher T2 value than muscle.

In the PD-weighted image (Figure 6.3), we observe the accurate depiction of fat as brighter and muscle as darker. In a PDw image, the signal recorded by the receiver coils is directly proportional to the proton density of each tissue. Fat, in this context, exhibits a higher proton density (i.e. number of protons per elementary volume) compared to muscle tissue, justifying the brighter signal representation.

In the case of the PDw image, it is noteworthy to mention that we endeavored to calculate the relative proton density between the two tissues. Rather than selecting a value from the literature, we aimed to select short TE and extrapolation to zero value of TE corresponding to the signal amplitude immediately after the RF pulse,which in turn is indicative of the proton density for each tissue. This idea remained unimplemented as we observed certain limitations with the SE sequence utilized in MRiLab

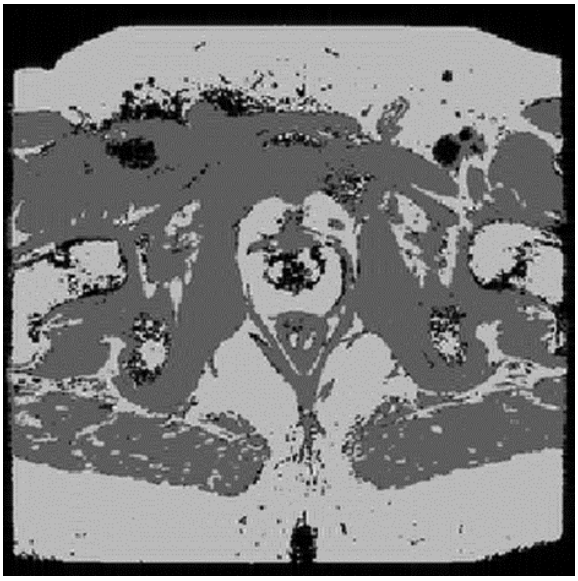

Figure 6.3: The SE-PDw Image (TE=10ms, TR=3500ms, flip angle=90 degree) of the male pelvic phantom. The signal intensity is directly proportional to the proton density of each tissue, with fat displaying a notably higher proton density compared to muscle tissue. This results in the brighter appearance of fat and the darker representation of muscle in the image. The grayscale image is presented in a 256x256x2 format, and a 2D representation is illustrated.

for TE values below 10ms. Subsequently, a second phase of our investigation may involve a thorough examination and potential modification of the sequence to allow for a wider range of TE values. Nevertheless, we have successfully executed all the necessary scripts required for signal estimation, including the creation of regions of interest within each tissue and the subsequent signal calculation.

6.1.1 Scanning parameters

It is crucial to emphasize the significance of selecting the appropriate scanning parameters, as their incorrect choice can lead to artifacts in our final images. One noteworthy artifact we encountered during our experiments was the partial volume effect (Figure 6.4), which arose due to an erroneous selection of tissue thickness. In general, our experiments revealed that a slice thickness of 3mm was suitable for accurately depicting our phantom. An advantage of magnetic resonance imaging simulation is the familiarity it provides to users with various artifacts and their exploration and resolution. This familiarity aids in understanding and mitigating such issues.

Another important parameter was the selection of the appropriate NEX (Num-

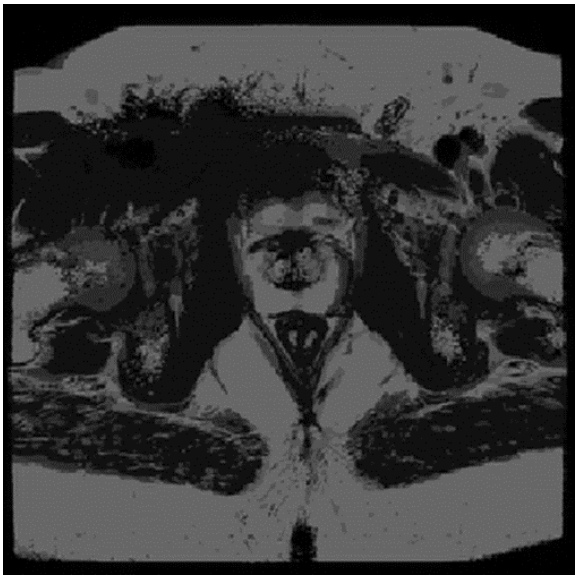

Figure 6.4: The phenomenon of Partial Volume effect due to erroneous choice of slice thickness. SE-T1w image (TE=20ms, TR=450ms) with 6mm slice thickness selected for imaging. The grayscale image is presented in a 256x256x2 format, and a 2D representation is illustrated.

ber of Excitations). Increasing the NEX value results in the accumulation of more signals from the same anatomy, which can enhance the Signal-to-Noise Ratio (SNR). This means that the image will have improved quality and clarity because the MRI machine averages the data from multiple acquisitions, reducing random noise. For SE sequences we used NEX=3 and for GRE images we used NEX=1.

6.2 Basic Image Analysis

Upon concluding the scanning process, the acquired data can be stored in the mat file format, affording us the flexibility to conduct analysis. While the scope of this thesis does not encompass image analysis, we will introduce fundamental concepts that have surfaced, offering simplified explanations to provide our readers with a comprehensive overview.

6.2.1 NEX and Entropy in SE-T2w Images

An intriguing concept arises in the exploration of entropy for the generated images. Entropy plays a crucial role in texture analysis, particularly when applied to grayscale images. In this context, grayscale images serve as a standard framework for entropy analysis. Entropy serves as a metric for gauging the degree of unpredictability and randomness present in the distribution of pixel intensities. In MRI, this is attributed to a variety of etiologies, including low SNR, inhomogeneity in the main magnetic field, non-uniform excitation, and improper choice of coils, among others. Elevated entropy values signify a broader range of pixel values, implying greater unpredictability, whereas lower entropy values indicate a more uniform and predictable texture.

To achieve this objective, we conducted a concise entropy analysis, calculating the mean entropy of SE-T2w images while varying the NEX parameter. Specifically, three SE-T2w images with dimensions of 256x256 and NEX values of 1, 2, and 3 were utilized. With the increase in the number of excitation (NEX), an enhancement in the signal-to-noise ratio (SNR) was noted. This improvement seems to us rational as the signal increased while the noise levels remained relatively constant. Consequently, this contributes to an overall enhancement in the signal-to-noise ratio, resulting in a clearer image. Moreover, we anticipated a decrease in the mean entropy of the images as the NEX parameter increased (Figure 6.5). We based this assertion on the premise that as the NEX parameter increases, resulting in improved image quality, the overall signal entropy is expected to decrease.The corresponding values of mean entropy and NEX are detailed in Table 6.2.

The diagram in Figure 6.5 validates our assertions; however, it is noteworthy that, as per existing studies in the literature, this behavior is predominantly observed for smaller values of NEX, specifically within the range of 1 to 3. It appears that for larger NEX values, the signal-to-noise ratio (SNR) tends to stabilize. This

Data Set	Mean Entropy	Std	NEX	SNR
Image 1	6.3004	0.0217	1	18.29
Image 2	6.2812	0.0228	2	25.84
Image 3	6.2779	0.0230	3	52.48

Table 6.2: This table presents three SE-T2w images (TE=90 ms, TR=3500 ms, RF flip angle= 90 degrees), each varying only in terms of the NEX parameter. The table includes the corresponding average entropy values for each NEX parameter.

observation prompts the need for further in-depth research and investigation. In this study, our objective was to provide a qualitative analysis of the produced images, demonstrating the fulfillment of expected fundamental principles.

6.2.2 Image Quality Assessment

The main focus of our analysis lies in the computation of metrics for the quality of the images we have generated. Image Quality Assessment (IQA) metrics have been developed and are used to quantify the degradation that an image undergoes after the application of forming, transforming, or enhancing algorithms. In this thesis, we utilized the PyTorch IQA Library [31], which encompasses a plethora of algorithms widely employed for research purposes. This library encompasses a diverse range of Image Quality Metrics (IQM), each designed to capture distinct aspects of image quality. These metrics can be classified into various categories. It is crucial to underscore the responsibility of users to select the appropriate IQA. The choice of metrics must align with the specific requirements of their problem. In our analysis, we employed the PSNR, SSIM, MS-SSIM, and FSIM metrics. The above metrics belong to the category of Full-Reference metrics, which are applicable when an undistorted reference image is accessible, enabling a direct comparison with the target image.

Peak-Signal-to-Noise-Ratio (PSNR): PSNR calculates the ratio between the maximum possible signal value and the power of the distorting noise affecting the quality of the examined image [32]. The mathematical representation of PSNR is given by the above equation:

$$\mathrm{PSNR} = 20 \cdot \log_{10} \left(\frac{\mathrm{MAX}_f}{\sqrt{\mathrm{MSE}}} \right) \tag{6.1}$$

In equation 6.1, $\mathrm{MAX_f}$ represents the maximum signal value of the reference

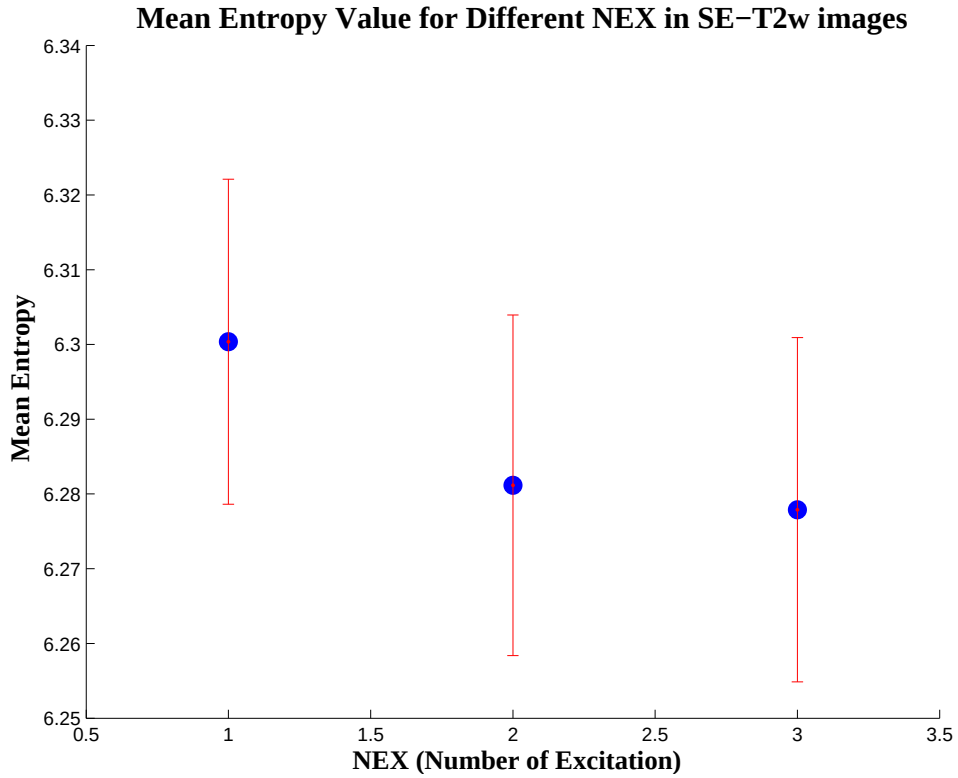

Figure 6.5: The diagram depicts the mean entropy as a function of NEX. The chart pertains to three SE-T2w images (TE=90ms,TR=3500ms, flip angle= 90 degree) with a resolution of 256x256, differing in the NEX parameter. The x-axis represents the NEX parameter, while the y-axis represents the mean entropy value for each image. We observe that the entropy value decreases as we increase the NEX number, which is logical. As we increase the NEX parameter, the Signal-to-Noise Ratio (SNR) also increases, resulting in reduced disorder or entropy in the image.

image, and MSE is the mean square error. Higher PSNR values signify smaller MSE, indicating that the testing image closely resembles the reference image.

Structural Similarity Index (SSIM): The SSIM method assesses image quality by considering structural image information [33]. The SSIM index incorporates three components: luminance (L), contrast (C), and structure (S). SSIM values, ranging from -1 to 1, indicate higher perceived image quality with higher SSIM values [34].

Multi-Scale SSIM (MS-SSIM): MS-SSIM serves as an extension to SSIM, encompassing variations in structural information across various scales. The term "scale" pertains to distinct levels of image resolution, elucidating why MS-SSIM involves a multi-resolution analysis of the image. SSIM is computed individually

at each scale, and the resulting SSIM values at each scale are combined. MS-SSIM values usually range from 0 to 1, with a value of 1 indicating perfect structural similarity between two images [34].

Feature Similarity Index Measure (FSIM): The FSIM evaluates similarity by comparing features extracted from the reference and testing images. It entails feature extraction and measures similarity based on these features. FSIM values range between 0 and 1, with higher values indicating a greater degree of similarity between the compared images [35].

For our analysis, we generated SE-T2w images with specific acquisition parameters (TE=90ms, TR=3500ms, RF flip angle=90 degrees). We introduced variations in resolution, creating images with dimensions of 192x192, 256x256, and 384x384 pixels. Within each resolution setting, we produced images with three different NEX values (NEX=1, NEX=2, NEX=3). NEX is an indirect measure of noise level, as it represents the number of times that one image is acquired for a single visualization. When NEX is greater than 1, it indicates that the image has been acquired multiple times. The final results are obtained by summing the acquisitions and dividing by the total number of acquisitions, contributing to noise reduction and improved image quality. Through this analysis, we aim to investigate the similarity of images under different NEX settings. The assessment was performed for each resolution imaging set, with the reference image chosen as the one with NEX=3, identified for its superior SNR in accordance with our discussion in the subsection 6.2.1.

Testing Image	Reference Image	PSNR	SSIM	MS-SSIM	FSIM
SE-T2w_192x192Res_1NEX	**SE-T2w_192x192Res_3NEX**	48.8914	0.9973	0.9998	0.9982
SE-T2w_192x192Res_2NEX	**SE-T2w_192x192Res_3NEX**	50.1138	0.9981	0.9998	0.9987
SE-T2w_256x256Res_1NEX	**SE-T2w_256x256Res_3NEX**	44.1517	0.9910	0.9991	0.9958
SE-T2w_256x256Res_2NEX	**SE-T2w_256x256Res_3NEX**	54.9819	0.9994	0.9999	0.9996
SE-T2w_384x384Res_1NEX	**SE-T2w_384x384Res_3NEX**	46.0049	0.9979	0.9992	0.9985
SE-T2w_384x384Res_2NEX	**SE-T2w_384x384Res_3NEX**	52.9127	0.9996	0.9998	0.9997

Table 6.3: This table presents scores for PSNR, SSIM, MS-SIM, and FSIM metrics, comparing each image to the reference image. We structured our analysis and metric calculations based on image resolution categories (192x192, 256x256, 384x384). Reference images were selected with NEX=3 due to their higher SNR, representing the best image quality among the three NEX values assessed. As illustrated in the table, each image with NEX=1,2 underwent a similarity examination with the reference image, and the corresponding metrics were computed. We observe a higher degree of similarity in images with NEX=2 and NEX=3. This observation indicates that irrespective of the matrix size (192x192, 256x256, 384x384), images tend to be more similar when the noise levels are closer.

The metrics results are presented in Table 6.3. It is evident that, regardless of the matrix size (resolution), images with NEX=2 and NEX=3 exhibit a higher degree of similarity compared to those with NEX=1 and NEX=3. Additionally, a notable improvement in SNR is observed when transitioning from NEX=1 to NEX=3. This

observation underscores the capability of similarity metrics to highlight noise levels as a significant factor in image similarity, given that all other parameters remain identical. This consistent finding holds true when pairs of images are designed with different matrix sizes, such as 192x192, 256x256, or 384x384. Moreover, this pattern persists across all four similarity metrics. Therefore, we conclude that, irrespective of resolution, images tend to exhibit greater resemblance when the noise level is similar.

CHAPTER 7

DISCUSSION AND FUTURE PERSPECTIVES

This thesis showcases the capability of utilizing simple image processing techniques to construct a digital male pelvis phantom that accurately reproduces human anatomy and mimics the behavior of human tissues in an MRI scanner. The initial focus of our study was on designing the phantom, mirroring the anatomy derived from corresponding MRI images. Tissue delineation involved segmentation and masking techniques, and the assignment of tissue properties relied on established values from the literature. Subsequently, we utilized the phantom for MRI simulation, implementing a fundamental MRI sequence (Spin Echo) with three distinct contrasts (T1w, T2w, PDw).

The versatility of our chosen technique for designing the phantom enables the representation of any anatomical area, conferring a substantial advantage by empowering the generation of extensive datasets. This versatility is particularly advantageous, allowing us to produce medical images across diverse sequences and protocols. The resultant data holds significant potential for numerous research studies spanning the domains of physics, artificial intelligence, and medical imaging analysis.

7.1 Future Perspectives

Initially, it would be particularly interesting to refine our phantom, thereby completing a task that has already commenced. It is essential to utilize masks derived from an improved segmentation method for the precise delineation of each tissue on every slide. Additionally, we aim to employ parametric maps of T1, T2, T2*, and proton density to better mimic human tissues. Parametric maps are obtained from clinical MRI scanners and faithfully represent tissue parameter values. Lastly, in this study, we only examined the axial plane, and it would be beneficial to explore

both the sagittal and coronal planes. In this case, the mathematical approximation of BREP for representing tissue surfaces may also be taken into consideration.

As a future study, a challenging yet promising idea involves extracting radiomic features from our phantom images. The creation of computational human phantoms holds the potential to address variability concerns and contribute significantly to standardizing radiomic features within the realm of radiomic analysis.

In conclusion, the technique we develop for designing virtual human phantoms, coupled with the MRI simulator, stands as a robust platform capable of generating extensive datasets for diverse research endeavors. We are open to collaborative opportunities across various domains, ranging from training AI models to conducting research studies in the intricate realms of MRI physics and medical imaging.

BIBLIOGRAPHY

[1] J. Lakhoo, G. Khatri, R. F. Elsayed, V. Chernyak, J. Olpin, A. Steiner, V. S. Tammisetti, K. M. Sundaram, and S. S. Arora, "Mri of the male pelvic floor," *Radiographics*, vol. 39, no. 7, 2019.

[2] R. Schirra, "Theory of nmr spectroscopy."

[3] T. G. Maris, *Notes in Magnetic Resonance Imaging, Basic Physics*.

[4] J. Soto Alvarez, "Quantum-mechanical aspects of magnetic resonance imaging," *Revista Mexicana de Fisica*, vol. 63, pp. 48–55, 2017.

[5] R. Toffanin, G. Guglielmi, and M. Cova, "Fast mri methods for the clinical evaluation of skeletal disorders," 2011.

[6] M. L. Lipton, *Totally Accessible MRI*.

[7] "Phantom 101, dataspectrum."

[8] K. F. Stupic, M. Ainslie, M. A. Boss, C. Charles, A. M. Dienstfrey, J. L. Evelhoch, P. Finn, Z. Gimbutas, J. L. Gunter, D. L. Hill, *et al.*, "A standard system phantom for magnetic resonance imaging," *Magnetic resonance in medicine*, vol. 86, no. 3, pp. 1194–1211, 2021.

[9] D. Kaljuste and M. Nigul, "Evaluation of the acr mri phantom for quality assurance tests of 1.5 t mri scanners in estonian hospitals," *Engineering, Medicine*, 2014.

[10] Wikipedia, "Computational human phantom."

[11] W. Kainz, E. Neufeld, W. E. Bolch, C. G. Graff, C. H. Kim, N. Kuster, B. Lloyd, T. Morrison, W. P. Segars, Y. S. Yeom, M. Zankl, X. G. Xu, and B. M. W. Tsui, "Advances in computational human phantoms and their applications in

biomedical engineering - a topical review," *IEEE Transactions on Radiation and Plasma Medical Sciences*, vol. 3, no. 1, pp. 1–23, 2019.

[12] International Commission on Radiological Protection, *RADIATION PROTECTION, Recommendations of the International Commission on Radiological Protection, ICRP PUBLICATION 2, Report of Committee II on Permissible Dose for Internal Radiation.* Published for The International Commission on Radiological Protection: PERGAMON PRESS, 1959. ICRP Publication 2.

[13] R. H. Olsher and K. A. Van Riper, "Application of a sitting mird phantom for effective dose calculations," *Radiation Protection Dosimetry*, vol. 116, no. 1-4 Pt 2, pp. 392–395, 2005.

[14] J. V. Nüchtern, M. J. Hartel, F. O. Henes, M. Groth, S. Y. Jauch, J. Haegele, D. Briem, M. Hoffmann, W. Lehmann, J. M. Rueger, and L. G. Großterlinden, "Significance of clinical examination, ct and mri scan in the diagnosis of posterior pelvic ring fractures," *Injury*, vol. 46, no. 2, pp. 315–319, 2015.

[15] J. R. Moore, R. A. Pathak, C. Snowden, C. W. Bolan, P. R. Young, and G. A. Broderick, "Multispecialty retrospective review of the clinical utility of pelvic magnetic resonance imaging in the setting of pelvic pain," *Translational Andrology and Urology*, vol. 6, no. 6, pp. 1155–1158, 2017.

[16] M. Ghafoori, M. Alavi, and M. Aliyari Ghasabeh, "Mri in prostate cancer," *Iranian Red Crescent Medical Journal*, vol. 15, no. 12, p. e16620, 2013.

[17] M. Ghafoori, M. Alavi, and M. Aliyari Ghasabeh, "Mri in prostate cancer," *Iranian Red Crescent Medical Journal*, vol. 15, no. 12, p. e16620, 2013.

[18] J. P. Radtke, D. Teber, M. Hohenfellner, and B. A. Hadaschik, "The current and future role of magnetic resonance imaging in prostate cancer detection and management," *Translational Andrology and Urology*, vol. 4, no. 3, 2015.

[19] "Prostate cancer: Statistics," 2023. PhysioPedia.

[20] "The male pelvic floors." CancerNet.

[21] D. Cohen, J. Gonzalez, and I. Goldstein, "The role of pelvic floor muscles in male sexual dysfunction and pelvic pain," *Sexual Medicine Reviews*, vol. 4, no. 1, pp. 53–62, 2016.

[22] D. J. Griffiths, *Introduction to Electrodynamics.* Prentice Hall, 3rd ed., 2005.

[23] C. Salgueiro, J. Dantas, and L. Morgado, "Principles of nuclear magnetic resonance and selected biological applications," vol. 8, 2019.

[24] Y. Chen, S. J. Almarzouqi, M. L. Morgan, and A. G. Lee, "T2-weighted image," 2018.

[25] F. Del Grande, F. Santini, D. A. Herzka, M. R. Aro, C. W. Dean, G. E. Gold, and J. A. Carrino, "Fat-suppression techniques for 3-t mr imaging of the musculoskeletal system," *Radiographics*, vol. 34, no. 1, pp. 217–233, 2014.

[26] "Mangoviewer."

[27] F. Liu, *MRiLab v1.3 User Guide*, January 12 2017.

[28] H. Benoit-Cattin, G. Collewet, B. Belaroussi, H. Saint-Jalmes, and C. Odet, "The simri project: a versatile and interactive mri simulator," *Journal of Magnetic Resonance*, vol. 173, no. 1, pp. 97–115, 2005.

[29] T. Hackländer and H. Mertens, "A pc-based simulation of a clinical mr scanner," *Academic Radiology*, vol. 12, no. 1, pp. 85–96, 2005.

[30] F. Liu, J. V. Velikina, W. F. Block, R. Kijowski, and A. A. Samsonov, "Fast realistic mri simulations based on generalized multi-pool exchange tissue model," *IEEE Transactions on Medical Imaging*, vol. 36, no. 2, 2022.

[31] S. Kastryulin, J. Zakirov, D. Prokopenko, and D. V. Dylov, "Pytorch image quality: Metrics for image quality assessment," 2022.

[32] N. Instruments, "Peak signal-to-noise ratio as an image quality metric," 2013.

[33] J. Nilsson and T. Akenine-Möller, "Understanding ssim," *NVIDIA Technical Report*.

[34] Z. Wang, E. P. Simoncelli, and A. C. Bovik, "Multi-scale structural similarity for image quality assessment," 2003.

[35] M. S. U. Umme Sara, Morium Akter, "Image quality assessment through fsim, ssim, mse and psnr—a comparative study," *Journal of Computer and Communications*, vol. 7, March 2019.